Journal of Non-Newtonian Fluid Mechanics 257 (2018) 22–43

Contents lists available at ScienceDirect

Journal of Non-Newtonian Fluid Mechanics

journal homepage: www.elsevier.com/locate/jnnfm

Stationary and time-dependent numerical approximation of the lid-driven cavity problem for power-law fluid flows at high Reynolds numbers using a stabilized finite element formulation of the VMS type

A. Aguirre[a], E. Castillo[*,a], M. Cruchaga[a], R. Codina[b,c], J. Baiges[b]

[a] Departamento de Ingeniería Mecánica, Universidad de Santiago de Chile, Av Libertador Bernardo O'Higgins, Santiago 3363, Chile
[b] Universitat Politècnica de Catalunya, Jordi Girona 1-3, Edifici C1, Barcelona 08034, Spain
[c] CIMNE – Centre Internacional de Metodes Numerics en Enginyeria, Gran Capità S/N, Barcelona, 08034, Spain

ARTICLE INFO

Keywords:
Stabilized finite element method
VMS
High Reynolds numbers
Lid-driven cavity flow
Power-law fluid
Hopf bifurcation

ABSTRACT

In this work, a variational multiscale finite element formulation is used to approximate numerically the lid-driven cavity flow problem for high Reynolds numbers. For Newtonian fluids, this benchmark case has been extensively studied by many authors for low and moderate Reynolds numbers (up to Re = 10, 000), giving place to steady flows, using stationary and time-dependent approaches. For more convective flows, the solution becomes unstable, describing an oscillatory behavior. The critical Reynolds number which gives place to this time-dependent fluid dynamics has been defined over a wide range 7, 300 $\lesssim$ Re $\lesssim$ 35, 000, using different numerical approaches. In the non-Newtonian case, the cavity problem has not been studied deeply for high Reynolds number (Re > 10, 000), specifically, in the oscillatory time-dependent case. A VMS formulation is presented to be validated using existing results, to determine flow conditions at which the instability appears, and lastly, to establish new benchmark solutions for high-Reynolds numbers fluid flows using the power-law model. Obtained results show a good agreement with those reported in the references, and new data related with the oscillatory behavior of the flow has been found for the non-Newtonian case. In this regard, time-dependent flows show dependence on both Reynolds number and power-law index, and the unsteady starting point has been determined for all studied cases. It is determined that the critical Reynolds number (Re_c) that defines the first Hopf bifurcation for Newtonian fluid flow is ranged between 8,100 $\lesssim Re_c \lesssim$ 8, 250, whereas for power-law indexes $n = 0.5$ and $n = 1.5$, it is 7,100 $\lesssim Re_c \lesssim$ 7,200 and 18,250 $\lesssim Re_c \lesssim$ 18,500, respectively.

1. Introduction

Non-Newtonian fluid constitutive models abound in the literature due to their importance in many fields; typical known substances like sauces and concentrates in the food industry [1,2], cement paste and slurries in construction works [3,4] or even biological fluids such as blood and synovial fluids [5,6] are just a few examples of non-Newtonian fluids [7,8]. Some distinguishing features associated with non-Newtonian fluid flows have started to gain scientific interest in recent years due to their connection with industrial applications. Drag reduction properties [9,10] and the capability to enhance heat transfer [11–15] using viscoelastic, viscoplastic and pseudoplastic materials are now topics of intense research. For these reasons, the non-Newtonian behavior both in creeping and highly convective flows needs to be well understood, and even though this work does not address a specific application, it aims to understand the flow dynamics of power-law fluids at any given condition.

In the numerical simulation framework of generalized-Newtonian flows, the power-law model is the standard non-Newtonian model to evaluate new numerical methods with accepted benchmark results up to Re = 10, 000 [16,17]. For this reason, the known shortcomings such as the limited range of shear rates where fitted values of power-law and consistency indexes can be used, and the possibility of zero and infinity predicted viscosities [8,18], are not taken into account when testing the numerical schemes.

The lid driven cavity flow problem is commonly used as a benchmark for numerical methods due to its simple geometry but complex fluid dynamics behavior, and it has been carefully addressed by many authors [16,17,19–21], making it one of the most extensively studied numerical problems. On both Newtonian and non-Newtonian fluid

* Corresponding author.
E-mail addresses: alejandro.aguirre@usach.cl (A. Aguirre), ernesto.castillode@usach.cl (E. Castillo), marcela.cruchaga@usach.cl (M. Cruchaga), ramon.codina@upc.edu (R. Codina), jbaiges@cimne.upc.edu (J. Baiges).

https://doi.org/10.1016/j.jnnfm.2018.03.014
Received 14 September 2017; Received in revised form 21 March 2018; Accepted 22 March 2018
Available online 26 March 2018
0377-0257/

flows, most studies have good agreement in their results, showing steady solutions up to moderate Reynolds numbers ($Re \leq 10,\ 000$). However, until now there is no agreement on the flow dynamics at high Reynolds numbers, since the solution becomes time dependent and the flow describes an oscillatory behavior that needs robust numerical methods [22,23], and accurate time integration schemes [24]. The first Hopf bifurcation has been defined over a wide range of $7{,}300 \lesssim Re \lesssim 35{,}000$, in the Newtonian case.

Drag-reducing polymer solutions are usually shear-thinning, viscoelastic and either strain-thinning or strain-thickening [25]. However, in some cases, generalized-Newtonian models, as Cross or power-law, are able to properly describe the rheological behavior even for high Reynolds number flows, as we can see in [25,26] (and references therein), where experimental and numerical results are compared. From the numerical point of view, purely viscous flows have been recently used to understand the effect of the shear-thinning and shear-thickening nature on the turbulent structures of the flow [27–29], without forgetting that generalized non-Newtonian models are only approximations of more complex fluids, specially in the turbulent regime where the time scales of the flow decrease and approach the time scale of the fluid, with the corresponding increase of viscoelastic effects on the flow. The above remarks, motivates the study of power-law fluid flows to evaluate the effect of viscous non-Newtonian effects in the flow development, and specifically in the transition from steady to time-dependent flows via Hopf bifurcation, and in the transition from laminar to chaotic flows. The aim to study high Reynolds numbers cases has been motivated because many industrial settings (different heat exchangers, bearing, centrifuges, drill string, etc.) are typically turbulent [28,29]. Although three-dimensional studies are relevant in many applications, bidimensional analyses are usually reported in the literature to test numerical formulations and to study complex vortex pattern formation when the Reynolds number encreases. From such analyses critical Reynolds numbers are determined to characterize flow instabilities. In the present work, the analysis of bidimensional cases is performed to establish the flow conditions at which the instability appears when the non-Newtonian power-law model is applied. Three-dimensional cases are out of the scope of the present work, nevertheless, the results obtained using the proposed VMS formulation could be used as a guideline to understand different vortex pattern formation for future bi- or three-dimensional analysis, taking into account that even for moderate Reynolds numbers the solution should become three-dimensional, as is already well known for Newtonian fluids.

The Newtonian case has been carefully addressed by many authors, and different solutions were found using steady and time dependent approaches. In [24], the finite difference method with a staggered marker-and-cell mesh was used to define the first Hopf bifurcation. In that work, the influence of the time step size was discussed, and an exhaustive analysis of the dynamics of the flow was made through phase diagrams in different points at the corners. The critical Reynolds number that defines a time-dependent solution was set at $Re = 7,\ 308$. In that work, the author showed that the global attractor seems to be reached for Reynolds numbers up to $Re = 15,\ 000$, after that, the solution becomes chaotic. Similar results were presented in [30] using the finite difference method and in a multigrid solver with a cell-by-cell relaxation procedure, defining the Hopf bifurcation between $8,\ 000 \lesssim Re \lesssim 8,\ 100$. In [31], the finite element method was used to solve the lid-driven cavity problem with a Q2-P1 pair of elements and an eigenvalue analysis to define the critical Reynolds ($Re = 8,\ 000$) value that defines a time-periodic solution. In [22], the authors solved the cavity problem using a 2D streamfunction and vorticity formulation for the Navier-Stokes equations with a pseudo time derivative approach and very fine meshes. Steady results were reported up to $Re = 21,\ 000$, by using the Richardson extrapolation in an extremely fine mesh of 601×601, yet it was stated that the possibility of steady solutions on higher Re was still questionable. In [23], the authors solved the same cavity problem using the finite element method with unstructured meshes of 180×180. Oscillatory results were reported for $Re = 33,\ 000$ and $Re = 50,\ 000$, however, the critical Reynolds number that defines the beginning of this oscillatory behavior was not addressed. In that work the authors solved the problem using zero initial conditions for velocity and zero values for pressure, showing the robustness of their method. In [20], the authors used a compact fourth-order-accurate central difference scheme to investigate the possibility of computing steady solutions at higher Re, reporting results up to $Re = 35,\ 000$ using a 501×501 grid when computing stationary Navier-Stokes equations. In [21] the same problem was solved with the finite volume method using a QUICK scheme and the SIMPLE algorithm on an extremely fine non-uniform mesh of 768×768, reporting results up to $Re = 65,\ 000$.

In the non-Newtonian case, the lid-driven square cavity problem has not been studied deeply for high Reynolds numbers. In [16], the authors used a decoupling multiple-relaxation-time Lattice Boltzmann flux solver (MRT-LBFS) on a 151×151 mesh for power-law indexes of 0.5 and 1.5. Although many flow characteristics were defined up to $Re = 10,\ 000$, instability apparition was not addressed. In [17], the authors used the same multi-relaxation-time Lattice Boltzmann Method (MRT-LBM) to study the flow dynamics. They analyzed deeply the influence of both Reynolds number and power-law index on vortex structures. Results were computed up to $Re = 10,\ 000$, with n ranging between 0.25 and 1.75 on a uniform 256×256 mesh, and only steady solutions were reported. In [18] the authors used a three-field finite element formulation to solve non-linear viscosity fluids, showing results for the double lid-cavity problem up to $Re = 5,\ 000$ in steady flows, with n ranging between 0.4 and 1.8. In [32] size-dependent couple-stresses were examined by applying a stream function-vorticity finite difference formulation. The time dependent behavior of a non-Newtonian fluid flow was studied, and oscillatory results were reported for different Re as a function of a length scale parameter. However, as far as we know, for the non-Newtonian power-law model, no results have been reported for the time dependent case.

For high Reynolds numbers, any finite element formulation needs to be stabilized [33] due to the instabilities arising when convection dominates diffusion using reasonable mesh sizes. Likewise, pressure needs to be stabilized if one wishes to use equal velocity-pressure interpolation. In this work, a variational multiscale formulation (VMS) is presented and validated using existing steady state results. This formulation has been used in the Newtonian case in both laminar [34] and turbulent regimes [35] with satisfactory results. The novelty of the work is the time dependent analysis developed for the cavity problem using Newtonian, shear-thinning and shear-thickening fluid flows. Some of the presented results could define new benchmark solutions for high Reynolds numbers. As far as we know, this is the first work devoted to analyzing the oscillatory time-dependent behavior developed in the lid-driven cavity problem for non-Newtonian fluids at high Reynolds numbers.

The paper is organized as follows. In Section 2, the incompressible Navier–Stokes problem is presented, followed by a brief explanation of the power-law model for non-Newtonian fluids, and lastly, the VMS finite element formulation is used to solve the cavity problem and some numerical details are given. In Section 3, numerical results are presented for stationary and time dependent approaches, using both Newtonian and non-Newtonian models. Conclusions and remarks are outlined in Section 4.

2. Incompressible Navier–Stokes equations

2.1. Problem statement

Let Ω be the computational domain of $\mathbb{R}^d$ ($d = 2$ or $d = 3$) occupied by the fluid in the time interval $[0,\ t_f]$, assumed to be bounded and polyhedral, and let $\partial\Omega$ be its boundary. The incompressible and isothermal time-dependent Navier–Stokes equations, using the standard two-field approach, can be written as:

$$\rho\frac{\partial \boldsymbol{u}}{\partial t} + \rho\boldsymbol{u}\cdot\nabla\boldsymbol{u} - \nabla\cdot(2\eta\nabla^s\boldsymbol{u}) + \nabla p = \boldsymbol{f}, \qquad \text{in } \Omega,\ t\in\,]0,t_f[, \tag{1}$$

$$\nabla\cdot\boldsymbol{u} = 0, \qquad \text{in } \Omega,\ t\in\,]0,t_f[, \tag{2}$$

where $\boldsymbol{u}$ is the velocity field, p the pressure, $\boldsymbol{f}$ the vector of body forces,[1] η the apparent viscosity to be defined using a non-Newtonian model, which in the Newtonian case is identical to the dynamic viscosity, and $\nabla^s\boldsymbol{u}$ the symmetrical gradient of the velocity $\left(\nabla^s\boldsymbol{u} = \frac{1}{2}(\nabla\boldsymbol{u} + (\nabla\boldsymbol{u})^T)\right)$. Note that in the incompressible case, $\nabla\cdot\nabla^s\boldsymbol{u} = \Delta\boldsymbol{u}$. The above equations need to be solved together with initial and appropriate boundary conditions. For the sake of simplicity in the exposition, we will consider homogeneous boundary conditions $\boldsymbol{u} = \boldsymbol{0}$ on $\partial\Omega$.

2.2. Power-law model

In general, the viscosity may be dependent on the rate of strain as well as on the state variables, such as pressure and temperature. From the rheological point of view, long chain molecules give place to complex fluids highly dependent on the velocity gradient [36,37], that usually require additional differential equations.The non-Newtonian models abound in the literature due to their importance, since they are found in many science and engineering fields, being even more common than Newtonian fluids in some cases.

The simplest model to define a non-linear relation between shear-stresses and the rate of deformation, is the two parameter power-law model, that despite their known disadvantages related to the singular values of viscosity predicted for very low and high shear rates, it is used to understand more complex models, like Carreau or Herschel Buckley which is a combination of the Bingham model and the power-law. This model is defined in terms of the strain rate tensor $\dot{\boldsymbol{\gamma}} := \nabla\boldsymbol{u} + (\nabla\boldsymbol{u})^T$, specifically, its magnitude $\dot{\gamma} = \sqrt{\frac{1}{2}(\dot{\boldsymbol{\gamma}}:\dot{\boldsymbol{\gamma}})}$, as

$$\eta = m\dot{\gamma}^{n-1}, \tag{3}$$

where m represents the consistency index and n the power-law index. It is important to define the power-law Reynolds number used below as

$$\mathrm{Re} = \frac{\rho U^{2-n}L_c^n}{m} \tag{4}$$

being U and L_c are the characteristic velocity and length. Note that the classical expression of the Reynolds number is obtained when $n = 1$ and $m = \mu$, being μ the absolute viscosity.

2.3. Variational form

Let us introduce some notation in order to write the weak form of Eqs. (1) and (2). The space of square integrable functions in a domain ω is denoted by $L^2(\omega)$, and the space of functions whose distributional derivatives of order up to $l \geq 0$ (integer) belong to $L^2(\omega)$ by $H^l(\omega)$. The space $H_0^1(\omega)$ consists of functions in $H^1(\omega)$ vanishing on $\partial\omega$. The topological dual of $H_0^1(\omega)$ is denoted by $H^{-1}(\omega)$, the duality paring by $\langle\cdot,\cdot\rangle$, and the L^2-inner product in Ω (for scalars, vectors and tensors) is denoted by $(\cdot,\cdot)$. The integral of the product of two functions in a domain ω is denoted as $\langle\cdot,\cdot\rangle_\omega$. The subscript ω is omitted when $\omega = \Omega$. The norm in a space X is written as $\|\cdot\|_X$, with the subscript omitted when $X = L^2(\Omega)$.

Let $\mathcal{V} = (H_0^1(\Omega))^d$ and $\mathcal{Q} = L^2(\Omega)/\mathbb{R}$ be the spaces of the velocity and the pressure, respectively. If we denote $\mathcal{X} := \mathcal{V}\times\mathcal{Q}$, the weak form of the problem in the Newtonian case consists in finding $\boldsymbol{U} = [\boldsymbol{u}, p]$: $]0,t_f[\to\mathcal{X}$ such that the initial conditions are satisfied and

$$\rho\left(\frac{\partial \boldsymbol{u}}{\partial t}, \boldsymbol{v}\right) + \langle\rho\boldsymbol{u}\cdot\nabla\boldsymbol{u}, \boldsymbol{v}\rangle + 2\eta(\nabla^s\boldsymbol{u}, \nabla^s\boldsymbol{v}) - (p, \nabla\cdot\boldsymbol{v}) = \langle\boldsymbol{f}, \boldsymbol{v}\rangle, \tag{5}$$

$$(\nabla\cdot\boldsymbol{u}, q) = 0, \tag{6}$$

for all $\boldsymbol{V} = [\boldsymbol{v}, q] \in \mathcal{X}$, where it is assumed that $\boldsymbol{f}$ is such that $\langle\boldsymbol{f}, \boldsymbol{v}\rangle$ is well defined.

In compact form, the problem Eqs. (5) and (6) can be written as:

$$\rho\left(\frac{\partial \boldsymbol{u}}{\partial t}, \boldsymbol{v}\right) + B(\boldsymbol{u}; \boldsymbol{U}, \boldsymbol{V}) = \langle\boldsymbol{f}, \boldsymbol{v}\rangle, \tag{7}$$

where

$$B(\hat{\boldsymbol{u}}; \boldsymbol{U}, \boldsymbol{V}) = (2\eta\nabla^s\boldsymbol{u}, \nabla^s\boldsymbol{v}) + \langle\rho\hat{\boldsymbol{u}}\cdot\nabla\boldsymbol{u}, \boldsymbol{v}\rangle - (p, \nabla\cdot\boldsymbol{v}) + (\nabla\cdot\boldsymbol{u}, q).$$

Eq. (7) needs to be complemented with initial conditions satisfied in a weak sense. In the nonlinear case, the viscous term has to be replaced by $\langle 2\eta(\hat{\boldsymbol{u}})\nabla^s\boldsymbol{u}, \nabla^s\boldsymbol{v}\rangle$ and more regularity for the velocity needs to be required. This discussion is however outside the scope of this paper.

2.4. Galerkin finite element discretization and time discretization

The standard Galerkin approximation for the variational problem can be performed by considering a finite element partition $\mathcal{T}_h$ of the domain Ω. The diameter of an element domain $K \in \mathcal{T}_h$ is denoted by h_K and the diameter of an element partition is defined by $h = \max\{h_K | K \in \mathcal{T}_h\}$. Under the above considerations, we can construct conforming finite element spaces, $\mathcal{V}_h \subset \mathcal{V}$ and $\mathcal{Q}_h \subset \mathcal{Q}$ in the usual manner. If $\mathcal{X}_h := \mathcal{V}_h \times \mathcal{Q}_h$, and $\boldsymbol{U}_h = [\boldsymbol{u}_h, p_h]$, the Galerkin finite element approximation consists in finding $\boldsymbol{U}_h$: $]0, t_f[\to\mathcal{X}_h$ such that

$$\rho\left(\frac{\partial \boldsymbol{u}_h}{\partial t}, \boldsymbol{v}_h\right) + B(\boldsymbol{u}_h; \boldsymbol{U}_h, \boldsymbol{V}_h) = \langle\boldsymbol{f}, \boldsymbol{v}_h\rangle, \tag{8}$$

for all $\boldsymbol{V}_h \in \mathcal{X}_h$, and satisfying the appropriate initial conditions.

The standard option to discretize in time is the use of finite difference schemes. In particular we use for all cases a second order backward differencing scheme, based on:

$$\frac{\partial \boldsymbol{u}_h^{j+1}}{\partial t} = \frac{3\boldsymbol{u}_h^{j+1} - 4\boldsymbol{u}_h^{j} + \boldsymbol{u}_h^{j-1}}{2\delta t} + \mathcal{O}(\delta t^2), \tag{9}$$

where δt corresponds to the size of a uniform partition of the time interval $]0, t_f[$, while $\mathcal{O}(\cdot)$ represents the approximation order of the scheme. The superscript indicates the time step where the variable is being approximated, so that $\boldsymbol{u}^j$ is an approximation to $\boldsymbol{u}$ at time $t^j = j\delta t$.

2.5. Stabilized formulation

It is well know that Eq. (8) has numerical instabilities for high mesh Reynolds number problems, i.e., when the nonlinear convective term dominates the viscous term. Another drawback of this formulation is the discrete compatibility or inf-sup condition that must be satisfied by the $\mathcal{V}_h \times \mathcal{Q}_h$ pair in order to have a well-posed problem with bounded pressure [33]. Using $\boldsymbol{V}_h = \boldsymbol{U}_h$ in Eq. (8), it can be seen that B is not coercive in $\mathcal{X}_h$ and no control over p_h is obtained. These difficulties can be overcame by using a VMS approach as shown below, see [38] for a review.

Stabilized finite element methods modify the discrete Galerkin formulation of the problem by adding some terms designed to enhance stability without upsetting accuracy. The stabilized method used in this work is based on the VMS approach introduced in [39] for the scalar convection-diffusion problem. The basic idea is to approximate the effect of the components of the solution of the continuous problem that cannot be solved by the finite element mesh. In summary, a VMS method is based on the splitting of the unknowns $\boldsymbol{U}$ (continuous solution) in a finite element component $\boldsymbol{U}_h$, which can be resolved by the finite element space, and the remainder $\widetilde{\boldsymbol{U}}$, which will be called sub-grid

[1] Although the vector of body forces is zero for the study case, it is maintained for completeness to keep in mind where it should be considered in the residual-based stabilized formulation presented below.

scale. This is finally defined in terms of $\boldsymbol{U}_h$ in some way, maintaining the number of unknowns of the problem.

To define the stabilized finite element formulation, we needs some additional notation. Eqs. (1) and (2) can be written in compact form as $\mathscr{D}_t\boldsymbol{U} + \mathscr{L}(\boldsymbol{u};\boldsymbol{U}) = \boldsymbol{F}$, where $\boldsymbol{U} = [\boldsymbol{u}, p]$, $\boldsymbol{F} = [\boldsymbol{f}, 0]$, and defining the following operators

$$\mathscr{L}(\hat{\boldsymbol{u}};\boldsymbol{U}) = \begin{pmatrix} \rho\hat{\boldsymbol{u}}\cdot\nabla\boldsymbol{u} - \nabla\cdot(2\eta\nabla^s\boldsymbol{u}) + \nabla p \\ \nabla\cdot\boldsymbol{u} \end{pmatrix}, \tag{10}$$

$$\mathscr{D}_t\boldsymbol{U} = \begin{pmatrix} \rho\dfrac{\partial\boldsymbol{u}}{\partial t} \\ 0 \end{pmatrix}, \tag{11}$$

where $\hat{\boldsymbol{u}}$ is an auxiliary variable written to distinguish the velocity with the role of advection.

We will omit the details of the derivation of the stabilization method. In the context of the two-field Navier–Stokes problem, see [34,40], and in three-field formulation for non-Newtonian fluid flows see [18,41]. Here we just state the method for the problem defined by Eq. (7). After some approximations, this method consists in finding $\boldsymbol{U}_h$: $]0, t_f[\to\mathcal{X}_h$ such that

$$\rho\left(\frac{\partial\boldsymbol{u}_h}{\partial t}, \boldsymbol{v}_h\right) + B(\boldsymbol{u}_h;\boldsymbol{U}_h,\boldsymbol{V}_h) + \sum_K \langle\widetilde{\boldsymbol{U}}, \mathscr{L}^*(\boldsymbol{u}_h;\boldsymbol{V}_h)\rangle_K = \langle\boldsymbol{f},\boldsymbol{v}_h\rangle, \tag{12}$$

for all $\boldsymbol{V}_h\in\mathcal{X}_h$, where $\mathscr{L}^*(\boldsymbol{u}_h;\boldsymbol{V}_h)$ is the formal adjoint of the operator Eq. (10) without considering boundary conditions, which in its discrete version is given by

$$\mathscr{L}^*(\hat{\boldsymbol{u}}_h;\boldsymbol{V}_h) = \begin{pmatrix} -\rho\hat{\boldsymbol{u}}_h\cdot\nabla\boldsymbol{v}_h - \nabla\cdot(2\eta\nabla^s\boldsymbol{v}_h) - \nabla q_h \\ -\nabla\cdot\boldsymbol{v}_h \end{pmatrix}, \tag{13}$$

and $\widetilde{\boldsymbol{U}}$ is the sub-grid scale, which needs to be approximated. If $\widetilde{P}$ is the L^2-projection onto the space of sub-grid scales, the approximation we consider within each element is

$$\widetilde{\boldsymbol{U}} = \boldsymbol{\alpha}\widetilde{P}[\boldsymbol{F} - \mathscr{D}_t\boldsymbol{U}_h - \mathscr{L}(\boldsymbol{u}_h;\boldsymbol{U}_h)] = \boldsymbol{\alpha}\widetilde{P}[\boldsymbol{R}], \tag{14}$$

where $\boldsymbol{\alpha}$ is a matrix computed within each element and called matrix of stabilization parameters. Note that regardless of the definition of $\widetilde{P}$, the sub-scale defined with Eq. (14) depends on the residual of the finite element approximation ($\boldsymbol{R}$), and therefore the methods are consistent by construction. As notation, $\boldsymbol{R}_u$ represents the residual of the momentum equation and R_p the residual of the continuity equation. Based on [35,40,42], we define

$$\boldsymbol{\alpha} = \mathrm{diag}(\alpha_1\boldsymbol{I}_d, \alpha_2), \tag{15}$$

with $\boldsymbol{I}_d$ the identity on vectors of $\mathbb{R}^d$ and the parameters α_i, $i = 1, 2$, are computed as

$$\alpha_1 = \left[c_1\frac{\eta}{h_1^2} + c_2\frac{\rho|\boldsymbol{u}_h|}{h_2}\right]^{-1}, \tag{16}$$

$$\alpha_2 = \frac{h_1^2}{c_3\alpha_1}, \tag{17}$$

In these expressions, h_1 corresponds to a characteristic element length calculated as the square root of the element area in the 2D case and the cubic root of the element volume in 3D, and h_2 corresponds to another characteristic length calculated as the element length in the streamline direction. The constants c_i, $i = 1, 2, 3$ are algorithmic parameters in the formulation. The values used for linear elements are $c_1 = 12$, $c_2 = 2$ and $c_3 = 4$. These values of c_1 and c_2 are optimal for the approximation of the one-dimensional convection–diffusion equation, while $c_3 = 4$ has been shown experimentally to be optimal in previous works. For complex 2D and 3D problems, numerical experience is the only way to define it. In the Newtonian context, these values have proven to be robust in different problems and for different applications. Nevertheless, note that the precise values of the algorithmic constants may affect the error for a given mesh size, but the rate of convergence is unaffected. For higher order elements, the characteristic lengths h_1 and h_2 should be divided by r^2 and r, respectively, being r the order of the finite element interpolation.The stabilization parameters are computed at each integration point, and thus the physical properties to be employed in their evaluation depend on the fluid, and consequently the non-Newtonian behavior is contained in this definition.

Inserting Eq. (14), with $\boldsymbol{\alpha}$ given in Eq. (15), in Eq. (12), we get the following method: find $\boldsymbol{U}_h$: $]0, t_f[\to\mathcal{X}_h$ such that

$$\rho\left(\frac{\partial\boldsymbol{u}_h}{\partial t}, \boldsymbol{v}_h\right) + B(\boldsymbol{u}_h;\boldsymbol{U}_h,\boldsymbol{V}_h) + S_1(\boldsymbol{u}_h;\boldsymbol{U}_h,\boldsymbol{V}_h) + S_2(\boldsymbol{U}_h,\boldsymbol{V}_h) = \langle\boldsymbol{f},\boldsymbol{v}_h\rangle + R_1(\boldsymbol{u}_h;\boldsymbol{V}_h), \tag{18}$$

for all $\boldsymbol{V}_h\in\mathcal{X}_h$, where

$$\begin{aligned} S_1(\hat{\boldsymbol{u}}_h;\boldsymbol{U}_h,\boldsymbol{V}_h) &= \sum_K \alpha_1\left\langle\widetilde{P}\left[-\rho\frac{\partial\boldsymbol{u}_h}{\partial t} - \rho\hat{\boldsymbol{u}}_h\cdot\nabla\boldsymbol{u}_h + \nabla\cdot\eta\nabla^s\boldsymbol{u}_h - \nabla p_h\right], -\rho\hat{\boldsymbol{u}}_h\cdot\nabla\boldsymbol{v}_h - \nabla\cdot\eta\nabla^s\boldsymbol{v}_h - \nabla q_h\right\rangle_K, \\ S_2(\boldsymbol{U}_h,\boldsymbol{V}_h) &= \sum_K \alpha_2\langle\widetilde{P}[\nabla\cdot\boldsymbol{u}_h], \nabla\cdot\boldsymbol{v}_h\rangle_K, \\ R_1(\boldsymbol{u}_h;\boldsymbol{V}_h) &= \sum_K \alpha_1\langle\widetilde{P}[\boldsymbol{f}], \rho\hat{\boldsymbol{u}}_h\cdot\nabla\boldsymbol{v}_h + \nabla\cdot\eta\nabla^s\boldsymbol{v}_h + \nabla q_h\rangle_K. \end{aligned}$$

The standard way to compute $\widetilde{P}$ consist in taking $\widetilde{P} = I$ (the identity), leading to the ASGS (algebraic sub-grid scale) method. The option we favor is the known as the orthogonal sub-grid scale method (OSS) which is defined when $\widetilde{P} = P_h^{\perp} = I - P_h$, where P_h is the L^2 projection onto the appropriate finite element space. For the numerical analysis of the ASGS and the OSS methods for the linearized Navier–Stokes equations using the classical velocity-pressure formulation in Newtonian fluids, see [34,40], respectively. In [42,43] we also describe the possibility of taking the multiscales as time dependent. Even through this option is crucial when very small time steps are used, we will not consider it in this work.

2.6. Fully discrete and linearized problem

The problem to be solved defined in Eqs. (1) and(2) using the power-law model Eq. (3) has two sources of nonlinearity, namely, the convective term and the non-Newtonian behavior of the viscosity. When the equations defined by Eq. (18) are discretized using the finite element method, other nonlinearities appear because of the dependence of the stabilization terms on the velocity.

Different types of linearization schemes can be defined regardless of the stabilization method. The most standard is the fixed-point iterative scheme (Picard scheme), since it is stable for divergence free velocities. Another option would be a Newton–Raphson scheme or variants of it, as well as hybrid methods between Picard and Newton–Rhapson. In this work, the fixed point method has been used, showing robustness in both stationary and time-dependent cases. In particular, the stabilization parameters and non-Newtonian viscosity are computed with a given velocity guess and iteratively updated, also neglecting the velocity sub-

scale. If we denote with a double superscript the time step and iteration counter, the problem to be solved at time step $j+1$ to find the $i+1$ iterate of the unknowns is given by:

$$\rho\left(\frac{3\boldsymbol{u}_h^{j+1,i+1}}{2\delta t}, \boldsymbol{v}_h\right) + \langle \rho \boldsymbol{u}_h^{j+1,i}\cdot\nabla \boldsymbol{u}_h^{j+1,i+1}, \boldsymbol{v}_h\rangle + \langle 2\eta^{j+1,i}\nabla^s \boldsymbol{u}_h^{j+1,i+1}, \nabla^s \boldsymbol{v}_h\rangle \tag{19}$$

$$\begin{aligned} &- (p_h^{j+1,i+1}, \nabla\cdot\boldsymbol{v}_h) + \sum_K \alpha_1 \langle \widetilde{P}\,[\boldsymbol{R}_u], -\rho \boldsymbol{u}_h^{j+1,i}\cdot\nabla \boldsymbol{v}_h - \nabla\cdot\eta^{j+1,i}\nabla^s \boldsymbol{v}_h\rangle \\ &+ \sum_K \alpha_2 \langle \widetilde{P}\,[\nabla\cdot\boldsymbol{u}_h^{j+1,i+1}], \nabla\cdot\boldsymbol{v}_h\rangle_K = \langle \boldsymbol{f}, \boldsymbol{v}\rangle \\ &+ \rho\left(\frac{4\boldsymbol{u}_h^{j} - \boldsymbol{u}_h^{j-1}}{2\delta t}, \boldsymbol{v}_h\right), \\ (\nabla\cdot\boldsymbol{u}_h^{j+1,i+1}, q_h) &+ \sum_K \alpha_1 \langle \widetilde{P}\,[\boldsymbol{R}_u], -\nabla q_h\rangle = 0, \end{aligned} \tag{20}$$

for all $\boldsymbol{V}_h \in \mathcal{X}_h$, where converged values at a given time step have only the time step superscript and $\widetilde{P}$ is the identity in ASGS formulation and $P_h^{\perp}$ in the OSS method. The stabilization parameters are evaluated with $u^{j+1,i}$ and R_u with $u^{j+1,i+1}$, except for the advection velocity and the viscosity, which are computed at iteration i.

Algorithm 1 (see Appendix A) describes the flow of calculations associated with each method. Additionally, we add in the algorithm the possibility to use sub-relaxation through the parameter $0 < \beta \leq 1$.

3. Numerical results

In this section, the lid-driven cavity flow benchmark is used to evaluate the numerical performance of the VMS formulation presented in Section 2.5. This classical problem has been used to validate new numerical methods in both Newtonian and non-Newtonian cases over the years. Even though the problem geometry is simple, it shows an interesting multi-vortex fluid dynamics as the Reynolds number increases.

The lid-driven cavity problem features a 1×1 square cavity, with three walls set with non-slip boundary conditions (the vertical ones and the bottom one), while the top wall is defined as a fixed non-null velocity that drives the cavity flow, as shown in Fig. 1. Note that, using the characteristic length equal to one, the lid-velocity equal to one and the density equal to one, the Reynolds number is set as $|\mathrm{Re}| = |\frac{1}{m}|$ using Eq. (4).

It is well known that high Reynolds number flows give rise to velocity boundary layers that are difficult to approximate. In order to evaluate the grid dependence of the solution, three bilinear element meshes of $M_1 = 100 \times 100$, $M_2 = 180 \times 180$ and $M_3 = 250 \times 250$ quadrilateral elements were tested. The meshes are exponentially concentrated near the walls in order to achieve a high resolution description of the boundary layer, specially in the most convective cases. Since grid convergence is reached on the second mesh (M_2) for the higher Reynolds number, all numerical results showed in the section were solved with this mesh, unless otherwise stated. In Fig. 1 we can see the mesh M_2 and its detail of the top right corner, using a $\times$ 511 zoom. The smallest element is found in every corner, with sizes of $(2.5 \times 10^{-4}) \times (2.5 \times 10^{-4})$, $(4.5 \times 10^{-6}) \times (4.5 \times 10^{-6})$ and $(1.5 \times 10^{-7}) \times (1.5 \times 10^{-7})$, for meshes M_1, M_2 and M_3, respectively. Note that this mesh structure allows us to compute accurate results that agree with those found in the literature, and therefore, their results are comparable with those computed on meshes of 768×768 elements and more.

This section is subdivided in three parts: in Sections 3.1 and 3.2, a stationary approach is used to solve the Newtonian and power-law fluid flow, respectively, while in Section 3.3 a time dependent approach is used to analyze them.

Regarding the VMS formulation used in this work, two possibilities were defined in Section 2.5. The first one defined when $\widetilde{P} = I$ (ASGS) and the other when $\widetilde{P} = P_h^{\perp}$ (OSS). Both formulations give practically overlapped results for all solved cases.

Regarding to the possibility to use sub-relaxation, we found that this is crucial to reduce the number of non-linear iterations needed to solve the stationary case for $\mathrm{Re} > 10,000$. In the range $10,000 < \mathrm{Re} < 25,000$ a $\beta = 0.7$ is sufficient; however, for more convective cases the relaxation value was set as $\beta = 0.4$. In the time-dependent case, the problem is solved independently of the power index or Reynolds number without sub-relaxation.

3.1. Stationary Newtonian fluid flow

In this section we solve the lid-driven cavity problem with stationary computations to evaluate the robustness of the VMS formulation presented in Section 2.5, starting all cases from an initial condition of zero velocity and pressure along the domain. The streamlines shown in Fig. 2, from $\mathrm{Re} = 10,000$ to $\mathrm{Re} = 65,000$, agree with the reference values published in [19–23], whose results are obtained using different methods and grids. In the literature, stationary results for the Newtonian cavity problem can be found up to $\mathrm{Re} = 65,000$ [21].

The number of vortices and their emergence as a function of the Reynolds number is a frequently discussed topic when solving the cavity problem, since the flow shows a wide variety of patterns highly depending on this number. At low Reynolds numbers, the cavity problem is defined by a large vortex, named primary vortex (PV) for being the first and only one with such characteristics, and two small counter rotating vortices. Those vortices appear in the bottom right corner (BR1) and in the bottom left corner (BL1). As Re increases, another vortex appears near the top left corner (TL1), close to the moving lid at $\mathrm{Re} \approx 1,500$.These three vortices (BR1, BL1 and TL1) are called secondary vortices since they appear beside the primary vortex near

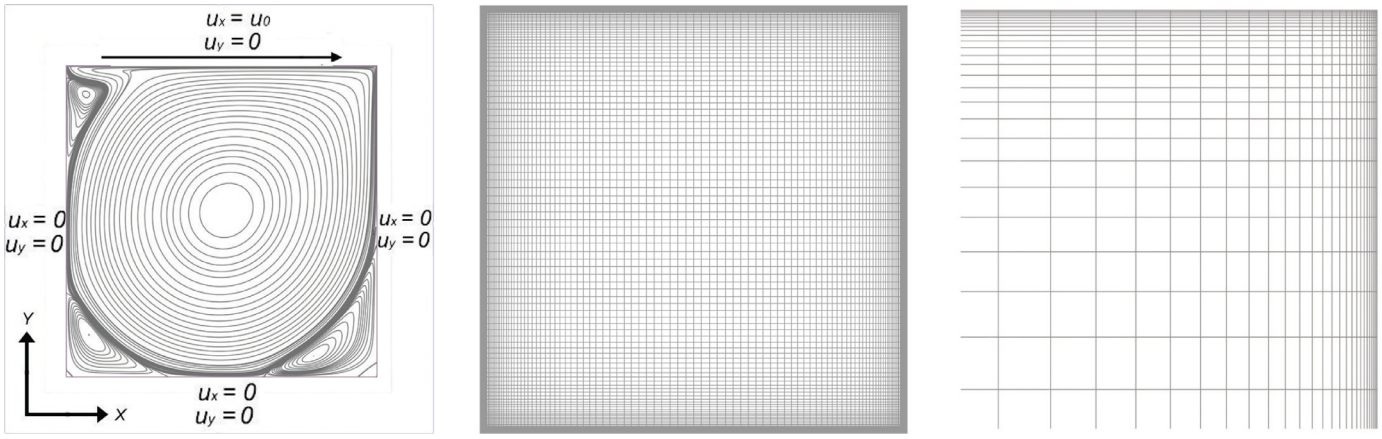

Fig. 1. From left to right, boundary conditions, mesh and mesh corner detail ($\times$ 511).

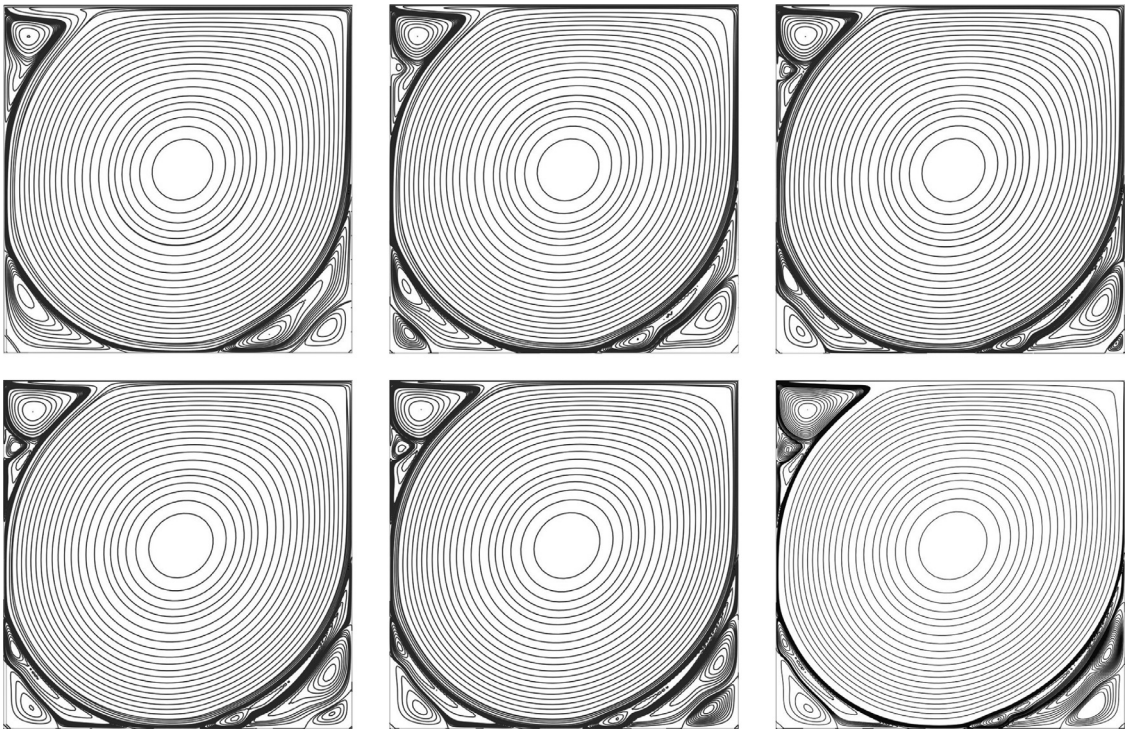

Fig. 2. Streamlines; from top-left to bottom-right: Re= 10, 000, 20, 000, 30, 000, 40, 000, 50, 000, 65, 000.

corners, but they are smaller and rotate in the opposite direction. As Re increases, the secondary vortices are displaced by another set of vortices, which counter rotates them, and start to emerge at Re ≈ 5, 000. These vortices appear in the same order and position as the secondaries, so they are called tertiary vortices, tagged as BR2 (Re ≈ 5, 000), BL2 (Re ≈ 10, 000) and TL2 (Re ≈ 15, 000). By now it is clear that as the Reynolds number increases, vortices appear near the corners of the cavity, so it is determined that the most suitable mesh for this problem would be a mesh that is exponentially concentrated near the walls. Note that the capability of the mesh to reproduce the small vortices can be crucial to define the flow patterns, and very important to determine the location of the other small vortices. By doing this we ensure a high resolution of the regions where the flow is most complex, letting us solve the cavity problem up to Re = 65, 000 without the need to increase dramatically the number of elements.

With the adopted mesh, it is possible to identify quaternary vortices at Re ≈ 10, 000 that do not reach an important size until Re ≈ 20, 000, and quinary vortices at Re ≈ 40, 000 that are still very small even at Re = 65, 000. In order to record information regarding vortices, Table 1, compares the position of the primary vortex and the secondary vortex BR1 with [21–23].

As usual, horizontal (u) and vertical (v) velocity profiles along the vertical and horizontal centerline are presented to validate the numerical method. In Figs. 3 and 4, the solutions obtained for the three meshes are compared with published results [19,21,23]. These velocity profiles are related to the capability to reproduce the velocity boundary layer and the dependence of the solution respect to the mesh. As we can see, the solution obtained with M_2 and M_3 are overlapped in all cases, and for this reason M_2 was selected as the recommended mesh.

A remarkable characteristic of the flow evolution showed in Figs. 3 and 4 is that both u and v velocity profiles along centerlines become sharper as the Reynolds number increases, which also denotes a high velocity gradient in the boundary layer that must be captured to define the flow properly. This tendency, however, slowly fades until those velocity profiles remain practically invariant for Re ≥ 30, 000. To illustrate this, Fig. 5 shows the velocity profiles along centerlines for cases of Reynolds numbers 5, 000 (dot lines), 33, 000 (dash lines) and 50, 000 (solid line). It can be seen that for Re = 33, 000 and 50, 000 the velocity profiles along centerlines are almost overlapped, while for Re = 5, 000 it shows a completely different boundary layer. This odd behavior may be an indicator of the vortex capabilities to dissipate energy and the presence of an instability, since the velocity seems to reach a convergence point, contrary to their flow patterns that keep developing and changing as Re increases. As we can see, the velocity profiles are important results to evaluate the convergence of the results, but they are not enough. Note that the flow patterns change (see Fig. 2

Table 1
Coordinates (x, y) of vortex centers.

Re		10,000	20,000	50,000	65,000
PV	Current	(0.5113, 0.5307)	(0.5097, 0.5264)	(0.5075, 0.5249)	(0.5076, 0.5249)
	[22]	(0.5117, 0.5300)	(0.5100, 0.5267)	(–)	(–)
	[23]	(0.5110, 0.5330)	(0.5080, 0.5280)	(0.5060, 0.5260)	(–)
	[21]	(0.5127, 0.5292)	(0.5102, 0.5266)	(0.5076, 0.5241)	(0.5076, 0.5241)
BR1	Current	(0.7702, 0.0578)	(0.7128, 0.0404)	(0.6533, 0.0287)	(0.6377, 0.0263)
	[22]	(0.7767, 0.0600)	(0.7267, 0.0450)	(–)	(–)
	[23]	(0.7670, 0.0594)	(0.7060, 0.0416)	(0.6540, 0.0309)	(–)
	[21]	(0.7745, 0.0590)	(0.7234, 0.0433)	(0.6540, 0.0251)	(0.6269, 0.0219)

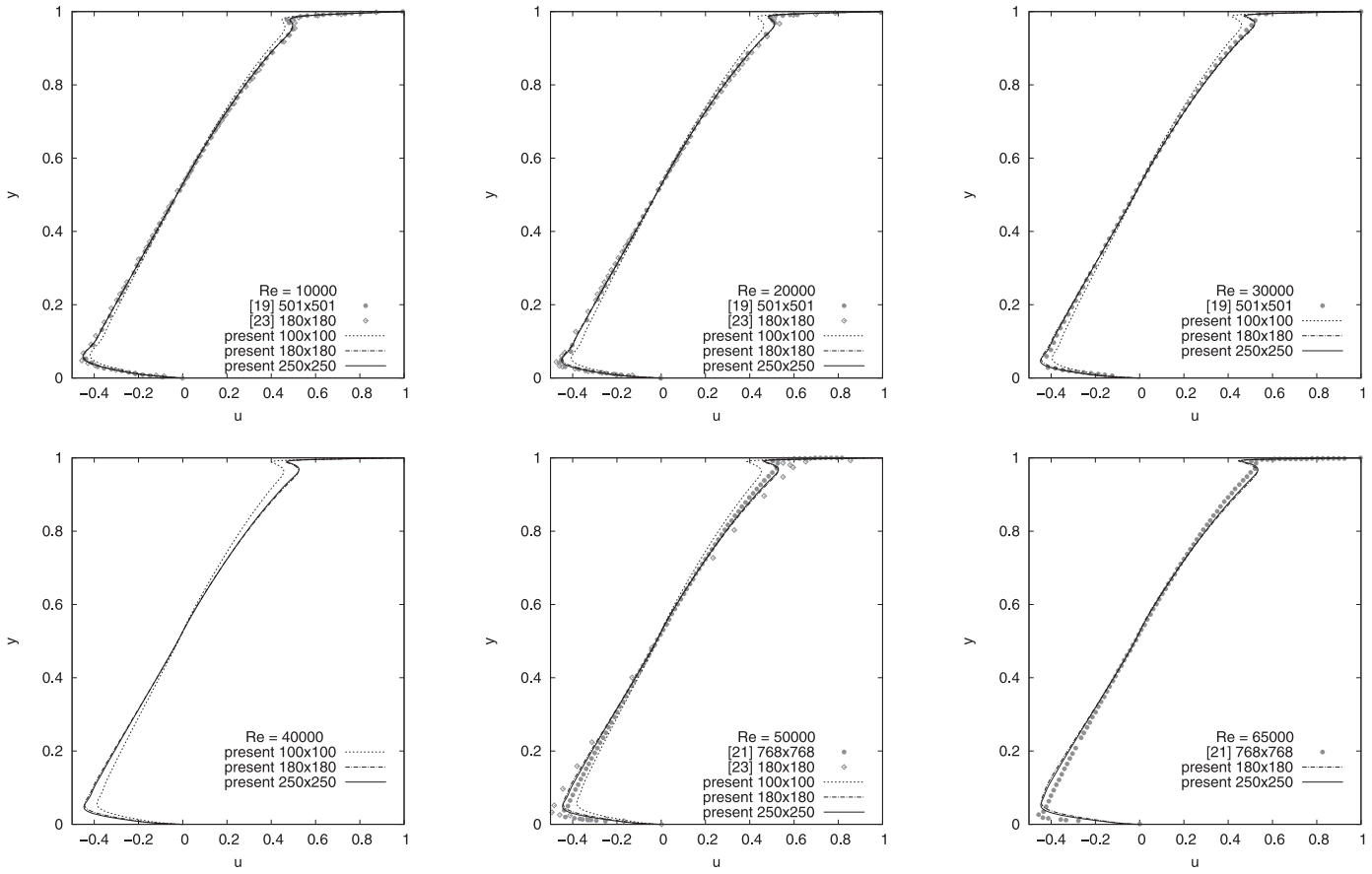

Fig. 3. u Velocity profile along $x = 0.5$.

for $30,000 < \mathrm{Re} < 65,000$), while the velocity profile is practically the same as shown in Fig. 5.

3.2. Stationary power-law fluid flow

In the previous subsection, the stabilized formulation was successfully validated for Newtonian flows, and here it is taken further to be applied in non-Newtonian fluids. In Newtonian fluids, the flow is only defined by the Reynolds number; however, in the non-Newtonian case, the power-law index can drastically modify the flow patterns.

In order to analyze the power-law index influence on the flow, it is ranged between $0.25 < n < 1.75$ for fixed Reynolds numbers of 500 and 5,000, whose u and v velocity profiles at the vertical and horizontal center lines of the cavity are illustrated in Figs. 6 and 7.

In general, pseudoplastic velocity profiles give place to lower velocities, that may be associated with a less convective flow; however, the boundary layer is sharper and narrower. This behavior makes sense since for pseudoplastic fluids viscosity tends to decrease the higher the shear rate is, and thus, the viscous effects are weaker than they are in the shear-thickening case, making the shear-thinning boundary layer to be narrow but the most sensitive to the shear stresses. This is an important point to be taken into account when analyzing nonlinear fluids, and gives information about the need to define very fine meshes near the walls.

Since the constitutive model of the fluid presented in this subsection describes a non-linear behavior, meshes used in the Newtonian cases may not be enough to correctly describe the flow dynamics. As usual, u and v velocity profiles at the centerlines of the cavity are used to evaluate grid dependence as well as to validate results. With regard to the mesh dependency, computations on meshes M_2 and M_3 give overlapped results in all cases, as illustrated in Figs. 8 and 9, hence those meshes are still valid even in non-Newtonian cases. A comparison with [16] shows good agreement of the velocity profiles, especially in dilatant cases. As Re increases, some differences appear, specially on the boundary layer of the shear-thinning fluids, that can be associated with the different meshes used for the same problem.

In order to properly illustrate the differences regarding the vortex development of each case, the appearance of the third secondary vortex (TL1) was compared with published results [16,17] to illustrate the importance of the exponential mesh for power-law fluids. This vortex was selected because the first one (BR1) and the second one (BL1) appear at low Re, and TL1 is the most practical to identify and compare. As seen in Figs. 10 and 11, TL1 appears at $\mathrm{Re} \approx 3,000$ for $n = 1.5$ and at $\mathrm{Re} \approx 1,500$ for $n = 0.5$. This comparison gives us an idea of how similar behaviors can manifest themselves at different Re values depending on the n index. According to the information provided in [17], those vortices appear at $\mathrm{Re} \approx 4,000$ and $\mathrm{Re} \approx 3,000$ for $n = 1.5$ and $n = 0.5$, respectively. It is clear that there are differences between each author, and we believe that the main reason is that some meshes are not able to correctly get the appearance of each vortex since they are smaller at the moment they appear. As far as we know, Newtonian studies of this case are mostly made on very thin meshes ranging

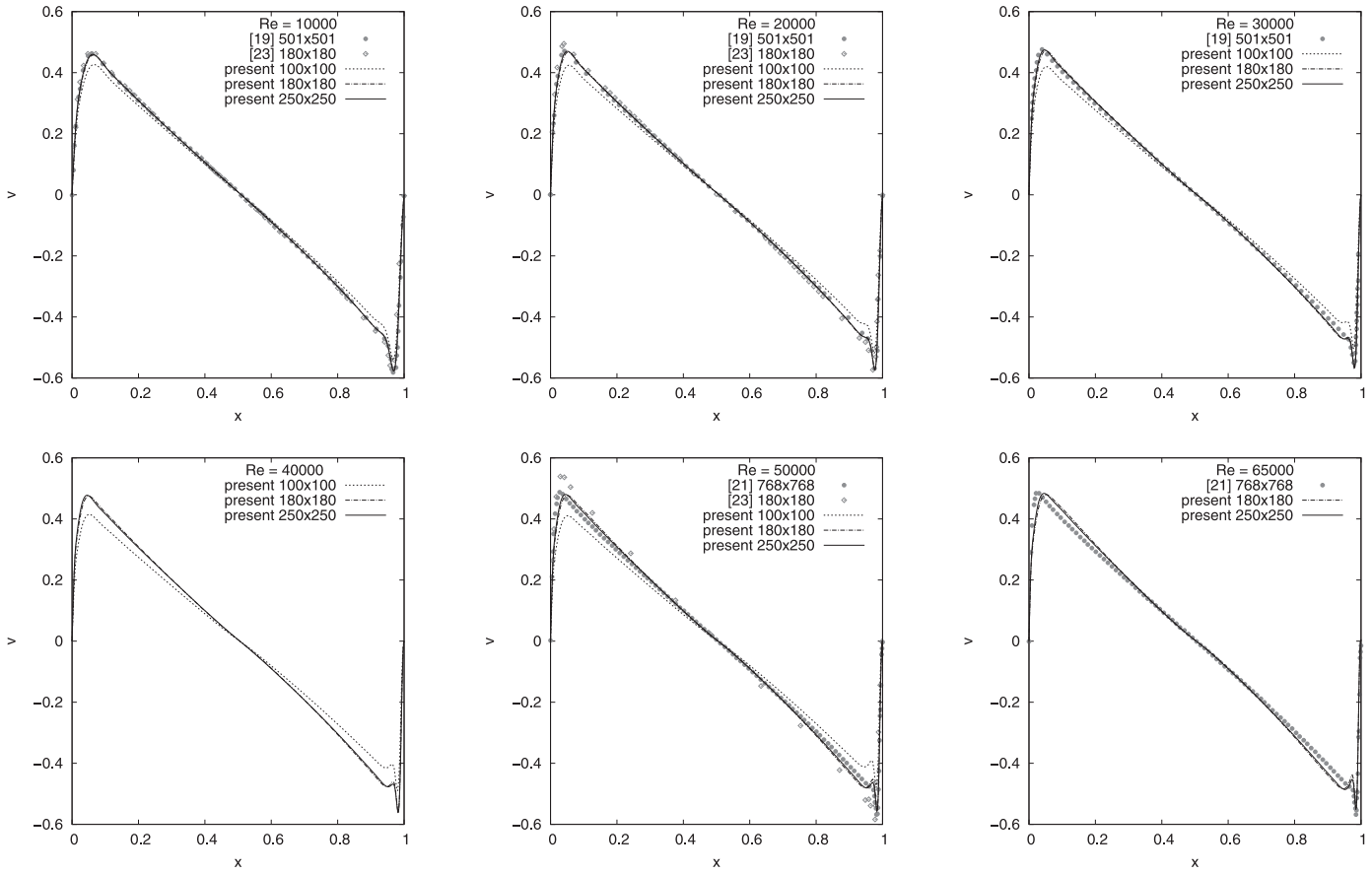

Fig. 4. v Velocity profile along $y = 0.5$.

between 500×500 [20] and 768×768 [21], while non-Newtonian studies use coarser meshes even when the fluid presents a non-linear behavior. Therefore, as seen above, a good agreement of the u and v velocity profiles is not enough to make an statement about the flow dynamics on high Reynolds numbers, since the appearance of the vortices needs to be considered, and it is highly dependent on the mesh.

Since it has been proved that n greatly influences the flow behavior, the increase of Reynolds number is the main issue, thus calculations are computed with $n = 0.5$ and $n = 1.5$. As mentioned in a previous section, Re is not defined as usual, but let us use the Newtonian case ($n = 1$) as a

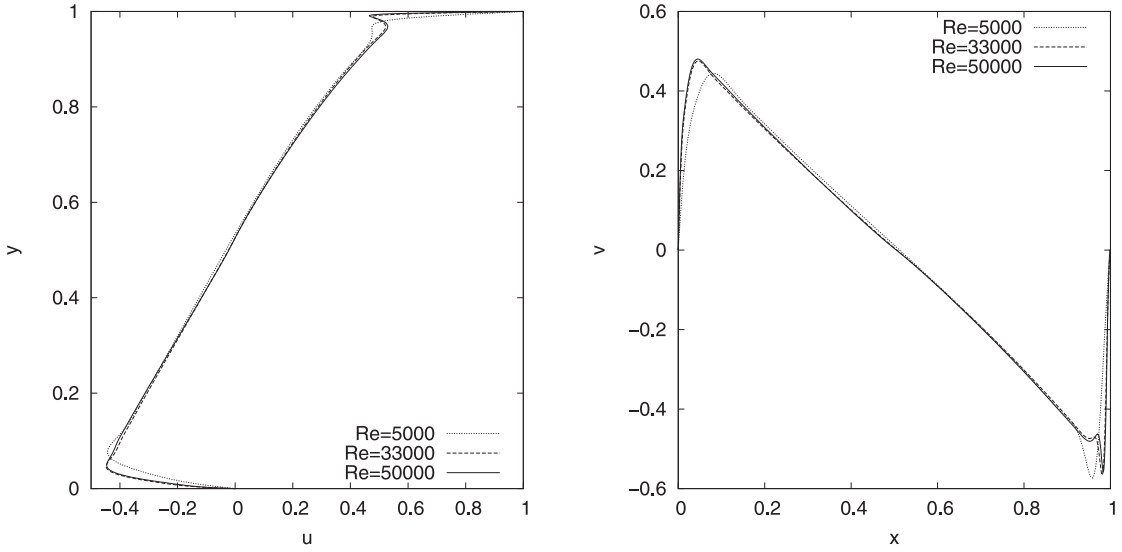

Fig. 5. u and v velocity profile comparison at $Re = 5,000,33,000,50,000$.

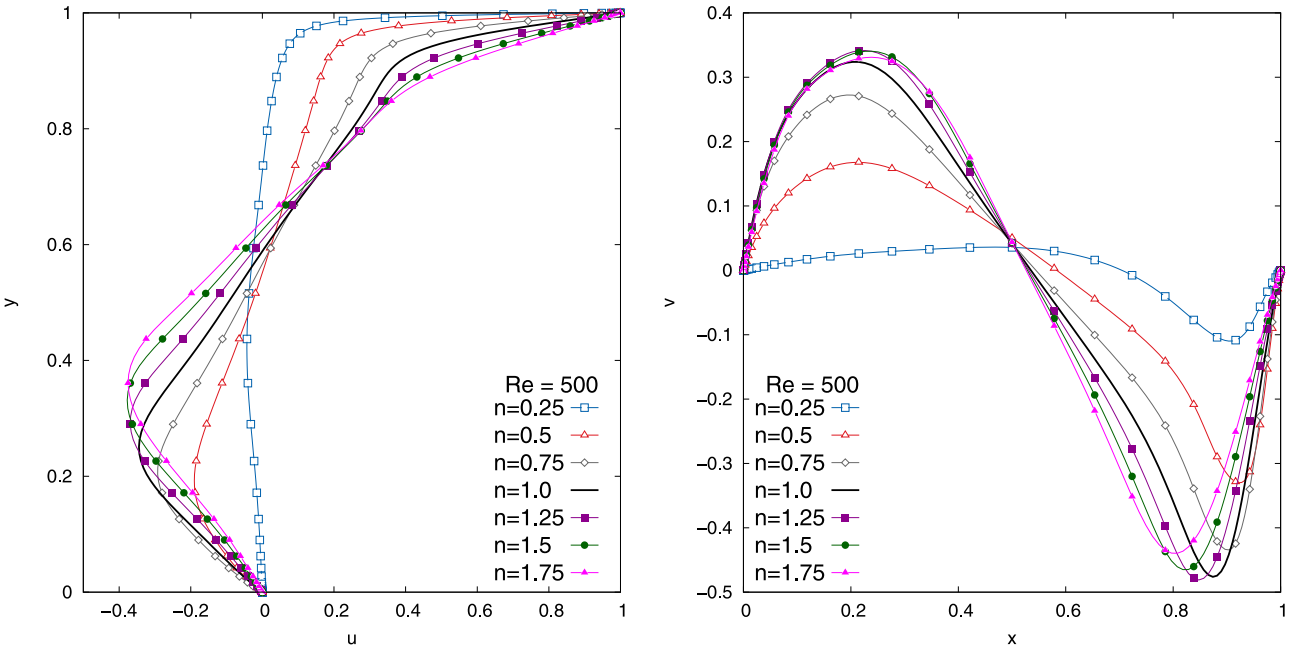

Fig. 6. u and v velocity profiles for $0.25 \leq n \leq 1.75$ along $x = 0.5$ and $y = 0.5$ at Re $= 500$.

reference. As far as vortices are concerned, they appear in the same order described in the Newtonian case, but at different Re depending on its power-law index. Compared to the Newtonian case, shear-thickening vortices appear at higher Re, yet still at close values, unlike shear-thinning ones that appear notoriously delayed. As a matter of fact, $n = 0.5$ computations barely reach tertiary vortices for the studied range, while $n = 1.5$ cases develop in a similar way the Newtonian one did. Figs. 12 and 13 show the streamlines of the appearance and evolution of each vortex as Re increases up to 40, 000. Note that stationary non-Newtonian simulations are able to compute even far beyond the said value, but since the scope of these computations is to study the possibility of time-dependent solutions, and hence to compare with time dependent results, they are not taken further. Still, Tables 2 and 3 present PV and BR1 centers locations, compared to published results by Li et al. [17].

The differences between the present work and the results published

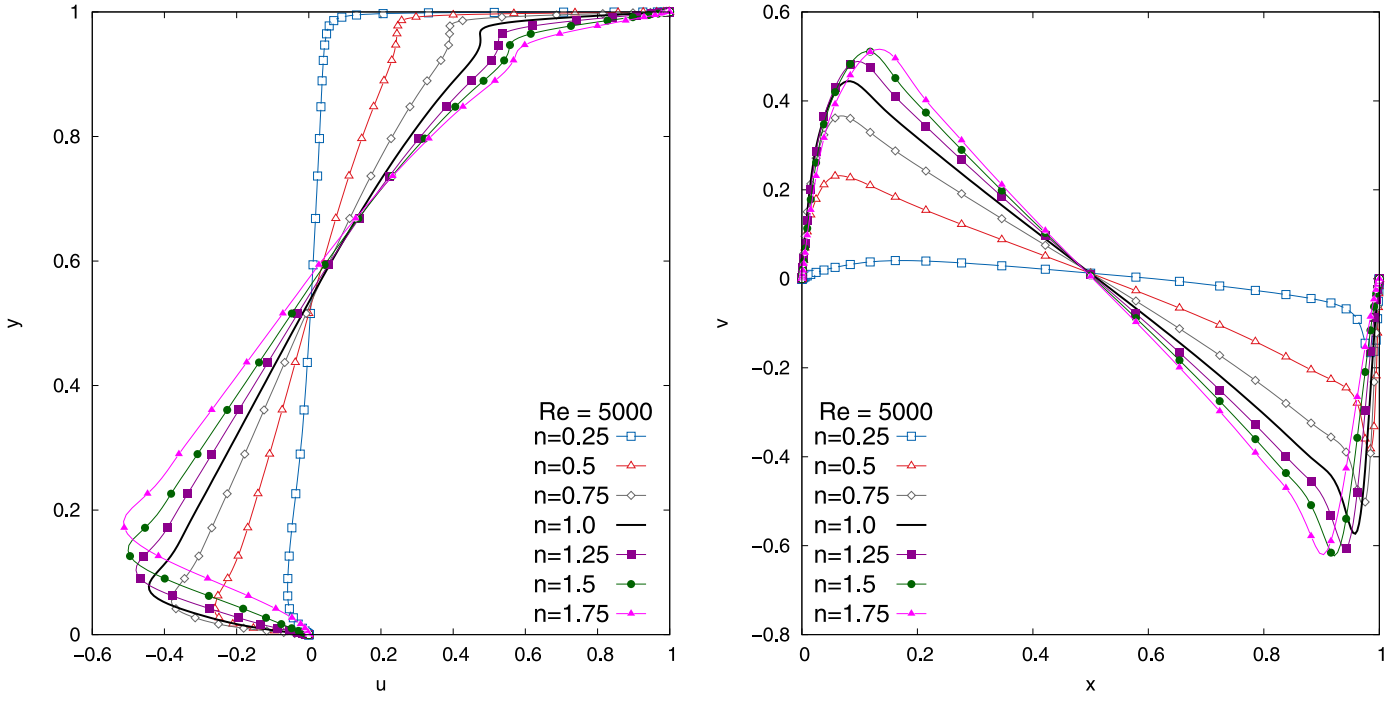

Fig. 7. u and v velocity profiles for $0.25 \leq n \leq 1.75$ along $x = 0.5$ and $y = 0.5$ at Re $= 5, 000$.

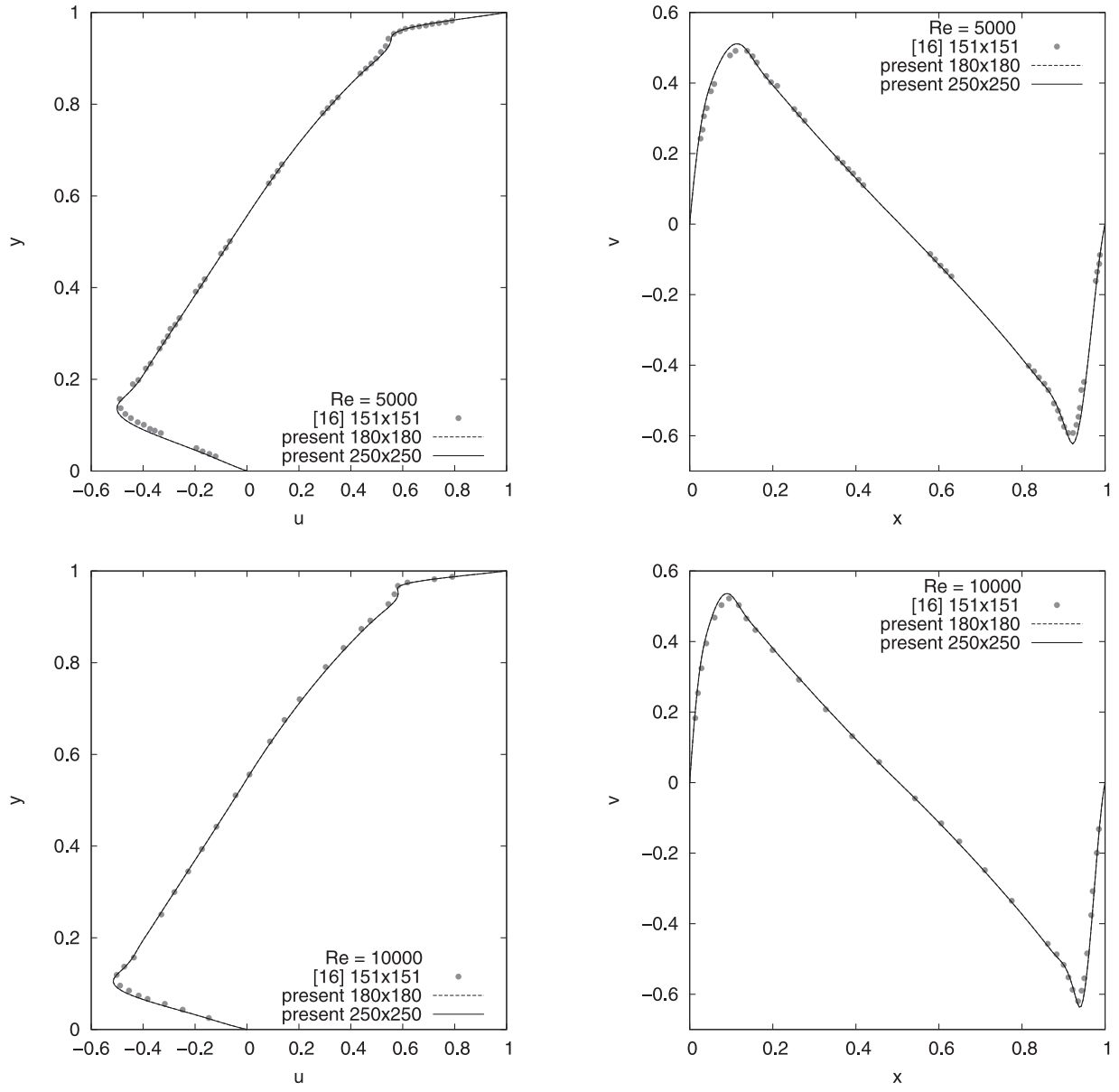

Fig. 8. u and v velocity profiles at Re = 5, 000 and Re = 10, 000 for $n = 1.5$.

by Li et al. [17] can be associated with the capability of the meshes to capture the appearance of the small vortices before, and therefore, the location is different. In Tables 2 and 3 the vortex location is presented for the cases that reach a steady state, which will be discussed in Section 3.3. We tested the three meshes M_1, M_2, M_3, and it was found that the coarser mesh of 100×100 showed a different vortex evolution compared to the other two finer meshes of 180×180 and 250×250, that presented the same evolution. The velocity profiles in the horizontal and vertical centerlines using different meshes is the standard method to verify mesh dependence, however, in order to check that vortices are mesh converged, v velocity profiles are plotted at $y = 0.02$ for Reynolds numbers 20, 000 and 30, 000, as presented in Figs. 14 and 15.

3.3. Time dependent flow

In this part of the work, the cavity problem is solved using a time-dependent approach to evaluate the critical Reynolds number at which the flow starts being time-dependent. Two different approaches are applied for this purpose. For the first one, the problem is solved sequentially using a continuation method, in the same way as [20,21]. For this approach, the problem is solved up to the steady state (if it exists) starting from Re = 5, 000. For more convective cases we use as initial condition the steady solution previously calculated. Note that this steady state solution may be unstable. The second approach consist in solving the problem with zero initial conditions for velocity, on each case up to the first case that shows an oscillatory time-dependent behavior.

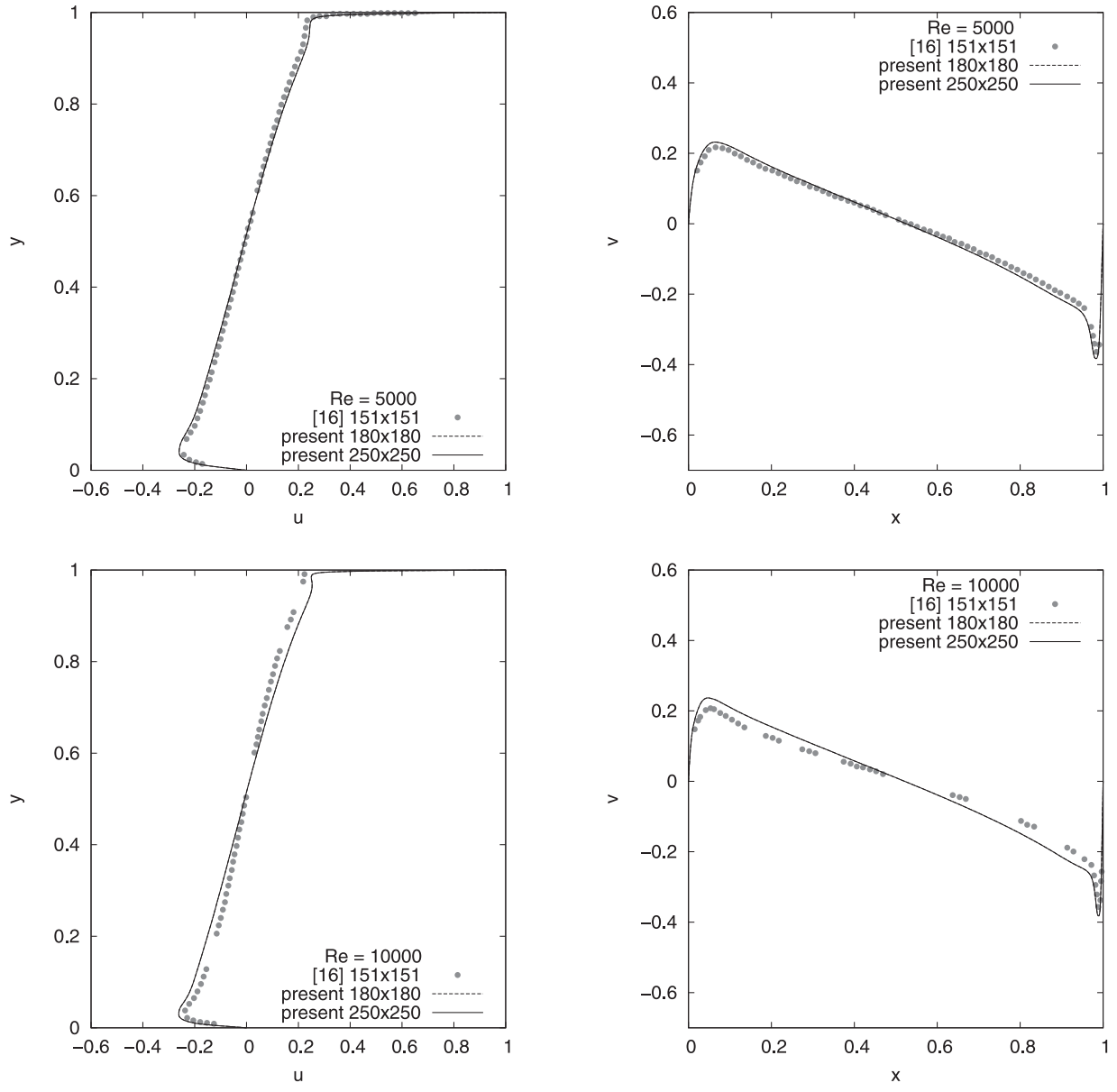

Fig. 9. u and v velocity profiles at Re = 5, 000 and Re = 10, 000 for $n = 0.5$.

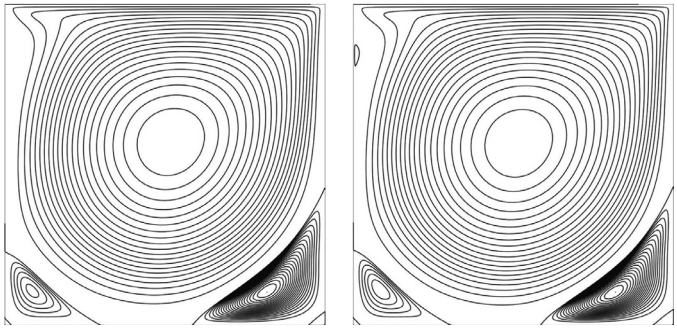

Fig. 10. Top left secondary vortex appearance for $n = 1.5$, between Reynolds number 2,500 and 3,000 from left to right.

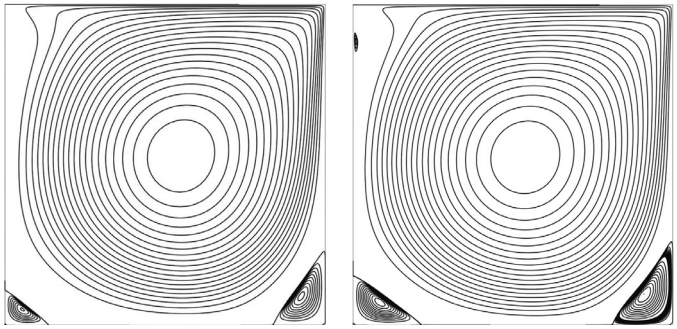

Fig. 11. Top left secondary vortex appearance for $n = 0.5$, between Reynolds number 1,000 and 1,500 from left to right.

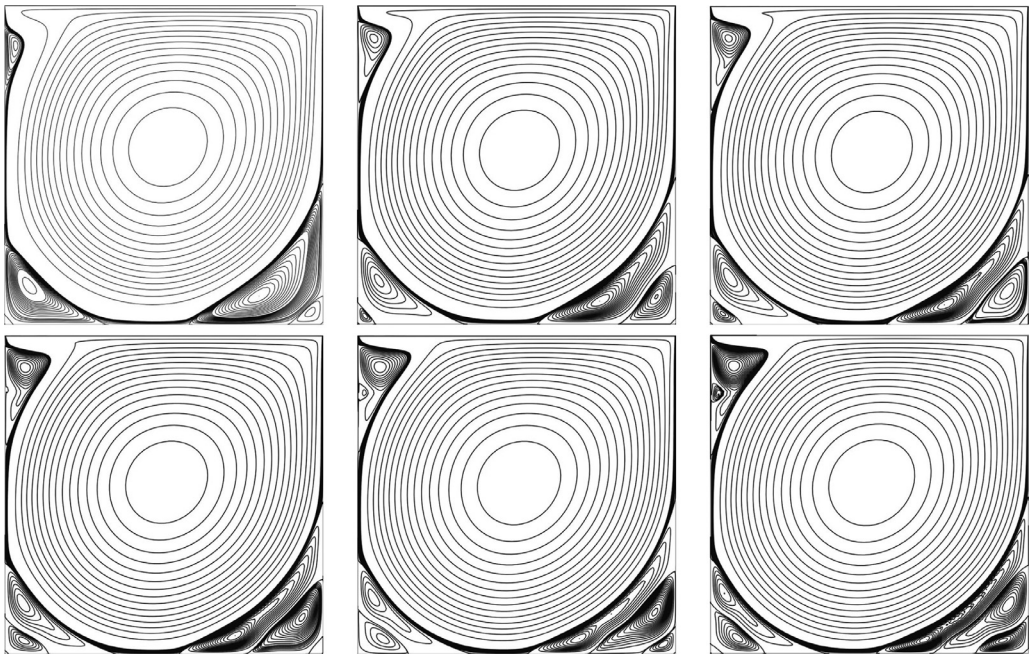

Fig. 12. Streamlines for $n = 1.5$ from top-left to bottom-right at Reynolds numbers: 5,000,10000,15000,20000,30000 and 40000.

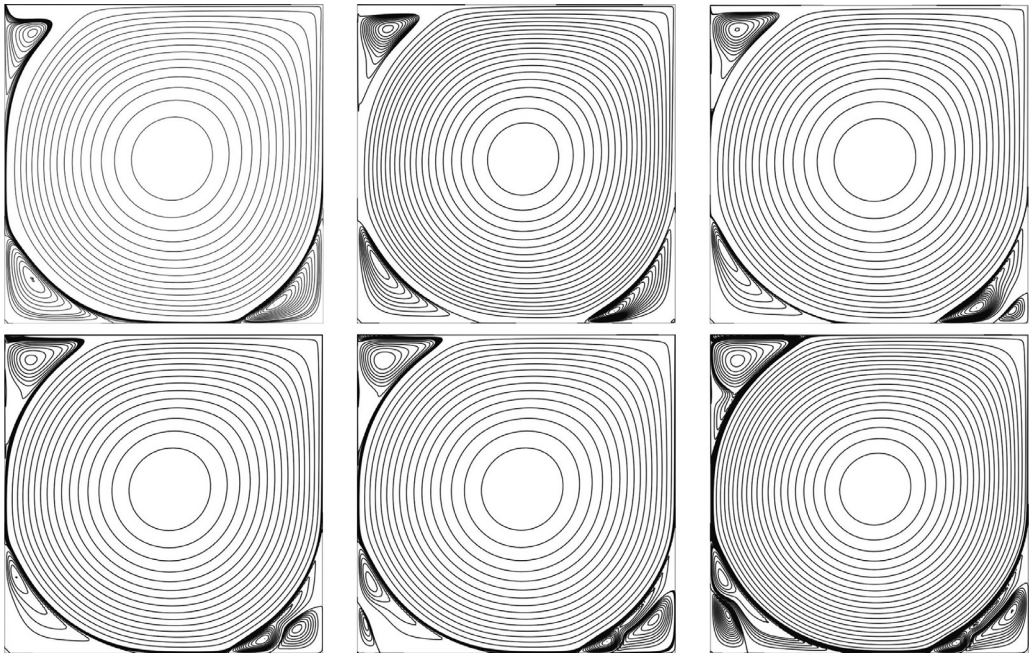

Fig. 13. Streamlines for $n = 0.5$ from top-left to bottom-right at Reynolds numbers: 5,000,10000,15000,20000,30000 and 40000.

The convergence in time is evaluated using two different time step values ($\delta t = 0.05$ and $\delta t = 0.025$) for solving the case Re = 10, 000. The obtained results are practically overlapped. Although the time step value $\delta t = 0.05$ reproduces the solution accurately, the number of points per period is considered insufficient to solve more convective cases, and for this reason, the selected time step was set as $\delta t = 0.025$ for all cases.

In the time-dependent approach, all flows need to develop up to the steady state or up to a time-dependent oscillatory behavior. At steady

state all vortex centers reach a fixed coordinate independent of time. Following this idea, the first Hopf bifurcation is encountered when vortices are not able to do so, following a time-dependent behavior. Is important to note that at the critical Reynolds value in which the bifurcation occurs, the solution may seem stationary if is not properly analyzed as it will be shown below. Regarding Newtonian fluid flow, the time-dependent computations using the continuation method converged to the same results given by the zero initial condition approach. At the same time, they reach the same steady states provided by the stationary computations presented in Section 3.1 up to Re = 8, 100. This is the last Reynolds number for which the two approaches give the same solution as those obtained in the stationary case; from this point on the flow becomes time-dependent. This result agrees with the results reported in [24,30,31,44], where the Newtonian case was exhaustively studied, and where the most important suggestion for the periodic behavior in the cavity problem was established. On the other hand, for the non-Newtonian case, the time-dependent solutions converged to the same steady results as the stationary cases described in Section 3.2, until different Re are reached depending on the fluid. For $n = 1.5$ the flow becomes time-dependent at a value ranged between 18, $250 \lesssim \mathrm{Re}_c \lesssim 18, 500$ while for $n = 0.5$ it happens at a value ranged between 7, $000 \lesssim \mathrm{Re}_c \lesssim 7, 200$, and any computation using higher Reynolds numbers gives unsteady results, being the lower limit the last steady solution obtained.

Regarding the dynamics of the problem, it is important to note that the primary vortex is practically fixed and the dynamics is developed near the walls between the secondary, tertiary, and quaternary vortices. The order in which the critical Reynolds number is found on each case is consistent with its fluid characteristics: the shear-thinning one, whose viscosity decreases at the boundary layer and has the sharpest velocity profile, is the first to get unstable, as opposed to the shear-thickening case, which gets oscillatory the latest. In Figs. 16–18, the streamlines associated to the first time-dependent case found are presented. For each case, a detailed view is presented for the tertiary and quaternary vortices at the corners (see the red boxes at the bottom corners of each global solution). Note that the presented vortices span at least 15

Table 2
Coordinates (x, y) of vortex centers for $n = 1.5$.

Re		5,000	10,000	15,000	20,000	30,000	40,000
PV	Current	(0.5281, 0.5162)	(0.5215, 0.5164)	(0.5212, 0.5157)	(0.5209, 0.5161)	(0.5197, 0.5161)	(0.5194, 0.5155)
	[17]	(0.5255, 0.5190)	(0.5347, 0.5183)	(–)	(–)	(–)	(–)
BR1	Current	(0.8544, 0.0648)	(0.8078, 0.0390)	(0.8431, 0.0519)	(0.8129, 0.0425)	(0.7858, 0.0357)	(0.7744, 0.0326)
	[17]	(0.8683, 0.0768)	(0.8595, 0.0588)	(–)	(–)	(–)	(–)

Table 3
Coordinates (x, y) of vortex centers for $n = 0.5$.

Re		5,000	10,000	15,000	20,000	30,000	40,000
PV	Current	(0.5146, 0.5568)	(0.5100, 0.5479)	(0.5081, 0.5431)	(0.5077, 0.5413)	(0.5065, 0.5408)	(0.5078, 0.5367)
	[17]	(0.5133, 0.5614)	(0.5098, 0.5502)	(–)	(–)	(–)	(–)
BR1	Current	(0.7999, 0.0914)	(0.7649, 0.0740)	(0.7429, 0.0638)	(0.7234, 0.0576)	(0.6957, 0.0483)	(0.6778, 0.0453)
	[17]	(0.8040, 0.0949)	(0.7763, 0.0787)	(–)	(–)	(–)	(–)

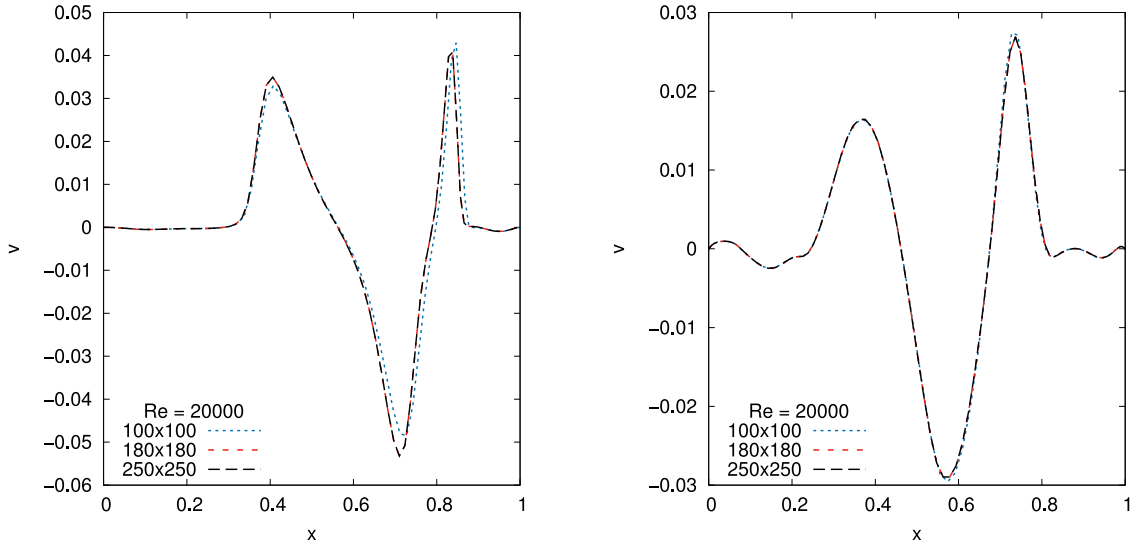

Fig. 14. v-velocity profiles at $y = 0.02$ and Re = 20, 000 for the three meshes, using $n = 0.5$ (left) and $n = 1.5$ (right).

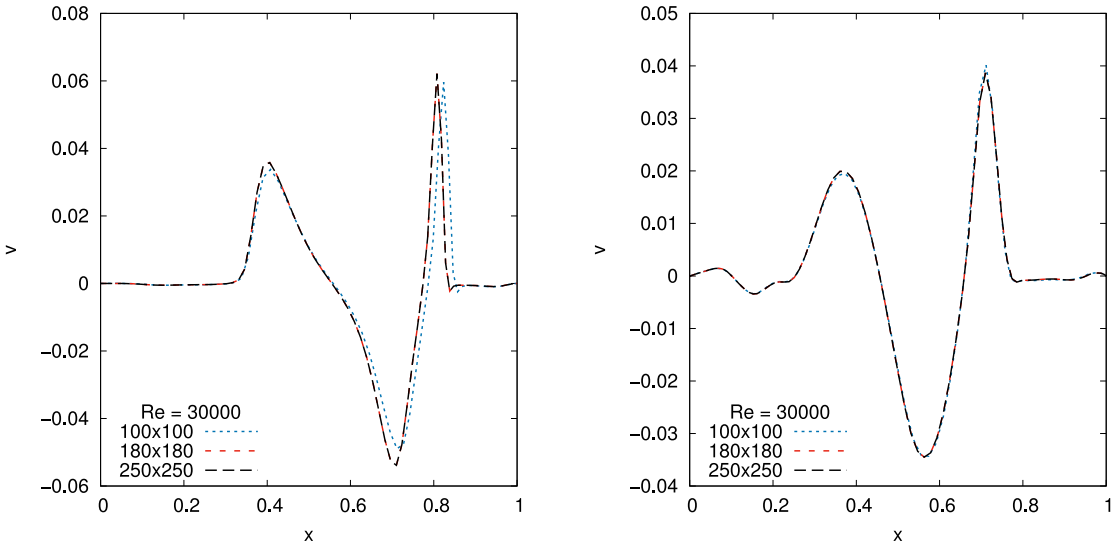

Fig. 15. v-velocity profiles at $y = 0.02$ and Re $= 30,000$ for the three meshes, using $n = 0.5$ (left) and $n = 1.5$ (right).

elements, yet the smallest vortices at the corners span at least 4 on each direction. At coordinates (0.05, 0.1), using the bottom left vertex as the zero reference, the point evolution history of the vertical velocity with its Fourier frequency spectrum and the phase diagram of velocity magnitude v/s pressure is plotted to illustrate the oscillatory behavior. At this point, there is only one frequency dominating the problem, and the phase diagram describes a closed path. The fundamental frequency found in the Newtonian case at Re $= 8,250$ is $f = 0.4437$; this result is in

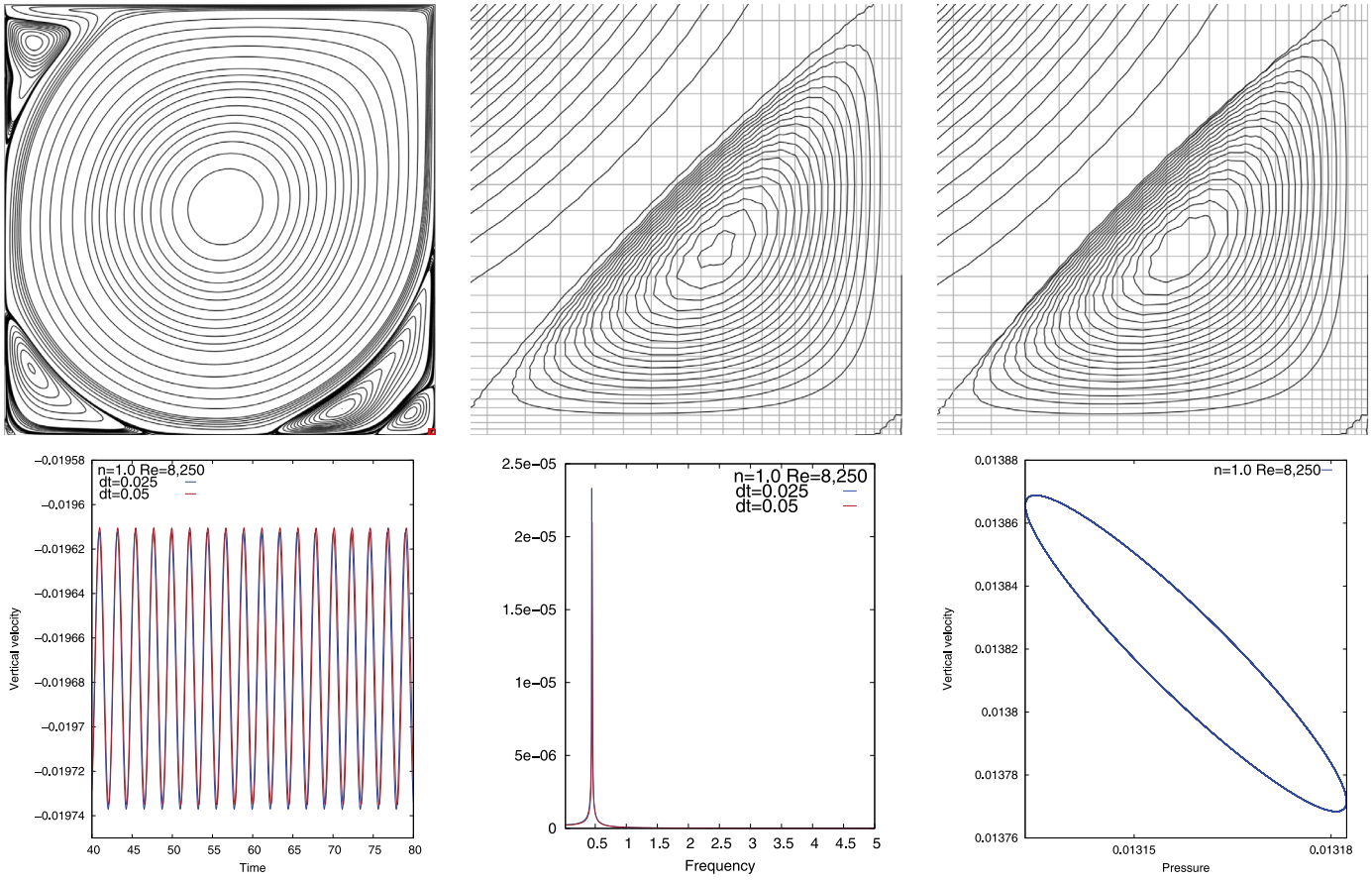

Fig. 16. Top: streamlines and quaternary vortex detail of the red box at two different times ($t = 59.2$ and $t = 59.9$), vertical velocity evolution (bottom left), FFT (bottom middle) and phase diagram (bottom right) at Re $= 8,250$ for $n = 1.0$. (For interpretation of the references to colour in this figure legend, the reader is referred to the web version of this article.)

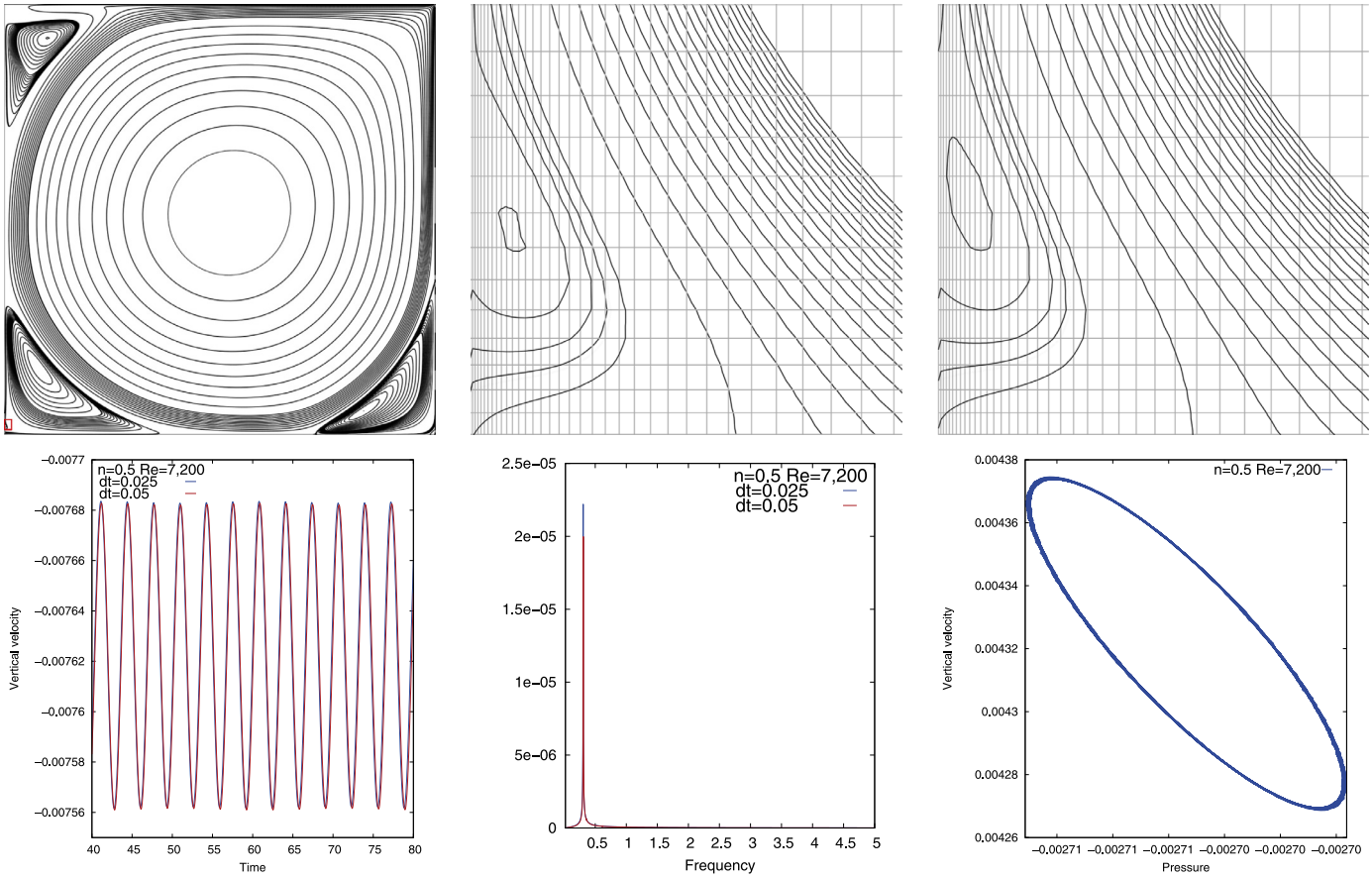

Fig. 17. Top: streamlines and tertiary vortex detail of the red box at different times (t = 51.7 and t = 52.5), vertical velocity evolution (bottom left), FFT (bottom middle) and phase diagram (bottom right) at Re = 7, 200 for n = 0.5. (For interpretation of the references to colour in this figure legend, the reader is referred to the web version of this article.)

good agreement with the results presented in [44,45], where a similar frequencies is found. In Figs. 16–18 the time convergence of the numerical approximations can be seen. Note that the tracking of the vertical velocity at a point located in (0.05, 0.1) and its fundamental frequency found for each case are practically the same both for $\delta t = 0.05$ and $\delta t = 0.025$. These results and the boundary layer plotted in Figs. 14 and 15, ensures the independence of the solution on the space-time discretizations reported in this work.

The streamlines associated to the first Hopf bifurcation may seem steady. However, the phase diagrams and the point evolution history show that the problem is time-dependent. This behavior can be described as a subtle throbbing of the second or higher order vortices, while the primary vortex remains unchanged. The detailed view illustrates the expansion and contraction of a small vortex located at the red square specified on each case. Similar results were reported for the Newtonian case in [24,30,31,46]. As far as we know, no time-dependent results have been reported in the non-Newtonian case. To summarize, Table 4 shows the interval for which the critical Reynolds numbers that define the first Hopf bifurcation are defined on each case. In this table, the critical Reynolds number ($\mathrm{Re_c}$), is defined in a range where the lower limit represents the last value for which the solution is steady ($\mathrm{Re_s}$) while the upper limit is the first Reynolds value for which the solution is dynamic ($\mathrm{Re_d}$). The last column shows the oscillatory frequency (f_d) at the upper limit.

For Reynolds numbers greater than $\mathrm{Re_d}$, the problem begins to be globally oscillatory, which can be seen in Figs. 19–21, where streamlines are plotted for four different times that describe an entire global oscillation (the zeros and peaks of a wave), for each fluid type. At Re = 10, 000 both Newtonian and pseudoplastic fluid flow have similar patterns. However, for the pseudoplastic case, more small amplitude frequencies were found active. Similar dynamics can be seen for Re = 20, 000 in the dilatant case, describing the shear-thickening behavior.

As the Reynolds number value increases, new frequencies appear in the frequency spectrum. For example, for the Re = 15, 000 Newtonian case (Fig. 22), a second frequency can be seen, which is a multiple (twice) of the fundamental frequency, a typical trend in oscillatory problems. The power-law index has a strong influence on the flow. In Fig. 23, the frequency spectrum and the phase diagram of a pseudoplastic fluid characterize a chaotic flow, while in the dilatant fluid, the

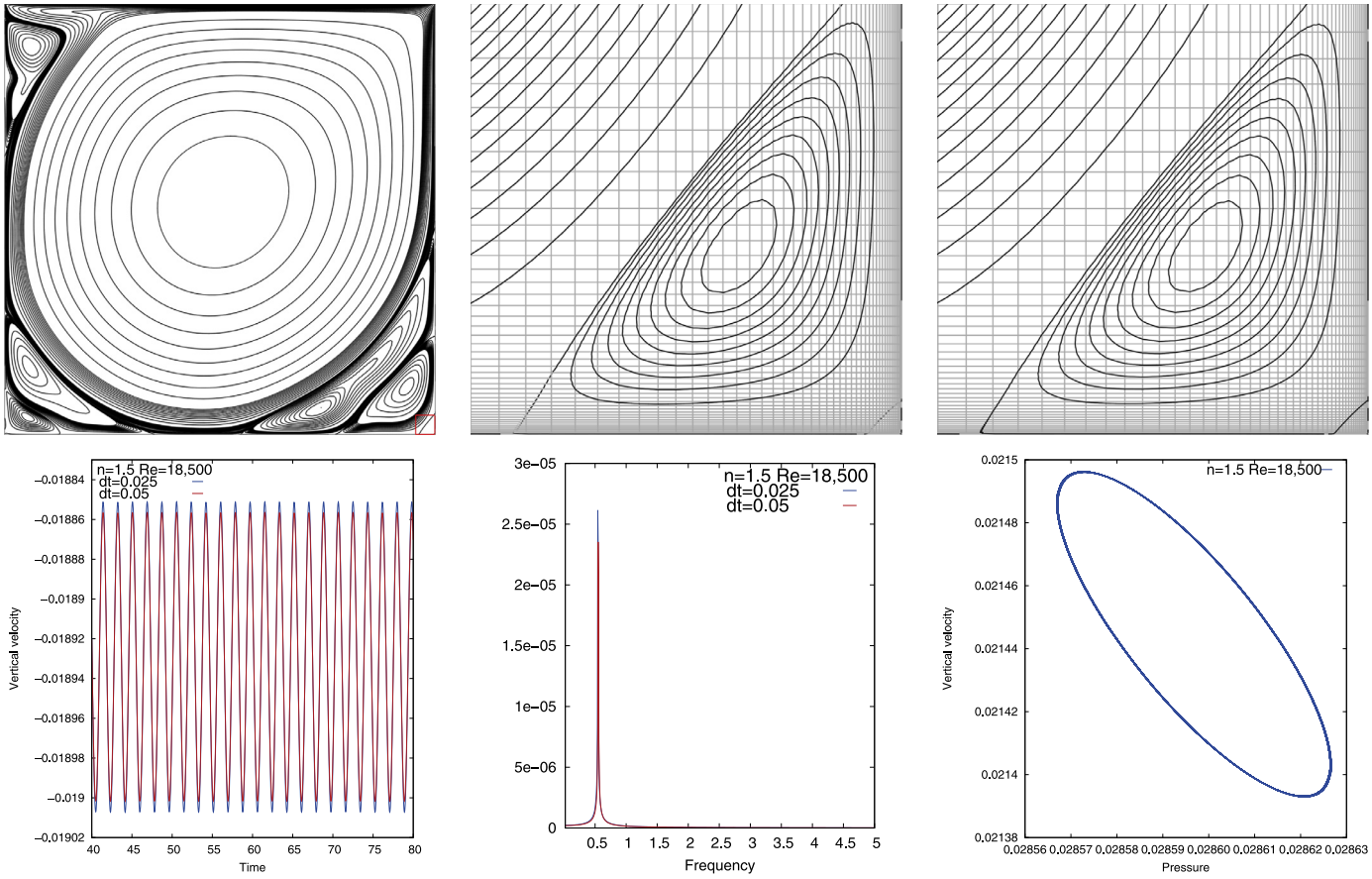

Fig. 18. Top: streamlines and quaternary vortex detail of the red box at different times ($t = 45.5$ and $t = 46$), vertical velocity evolution (bottom left), FFT (bottom middle) and phase diagram (bottom right) at $\mathrm{Re} = 18,\ 500$ for $n = 1.5$. (For interpretation of the references to colour in this figure legend, the reader is referred to the web version of this article.)

Table 4
Reynolds number of the first oscillatory computation for each fluid.

n	$\mathrm{Re_s} \lesssim \mathrm{Re_c} \lesssim \mathrm{Re_d}$	f_d
0.5	$7,\ 100 \lesssim \mathrm{Re_c} \lesssim 7,\ 200$	0.3062
1.0	$8,\ 100 \lesssim \mathrm{Re_c} \lesssim 8,\ 250$	0.4437
1.5	$18,\ 250 \lesssim \mathrm{Re_c} \lesssim 18,\ 500$	0.5438

solution is still dominated by the fundamental frequency with a closed phase diagram, as seen in Fig. 24.

For the Newtonian case, the problem becomes chaotic near $\mathrm{Re} = 20,\ 000$, as we can see in Fig. 25. In the frequency spectrum, many active frequencies have similar amplitudes and the phase diagram is not closed. In dilatant fluids, the second Hopf bifurcation that characterizes the beginning of chaotic flows is delayed. For the $n = 1.5$ case, the chaos starts near $\mathrm{Re} = 40,\ 000$ (Fig. 26), which makes us think that higher power-index values could lock the beginning of this behavior.

4. Conclusion

In this paper a VMS finite element formulation has been used to validate existing results found in the literature for Newtonian and power-law fluids in the cavity flow problem. The formulation proved to be robust enough to easily compute high Reynolds numbers flows in both stationary and time dependent approaches.

We have analyzed stationary and time-dependent cases, for both Newtonian and non-Newtonian fluids, in order to fully understand the influence of the power-law index for convective dominated cases. In the stationary cases, we proved that the u and v centerline velocity profiles are not enough to validate results, because the small vortices appearance is highly dependent on the mesh used and is not checked using those velocity profiles. This key point could be not important in the stationary case. However, to find the first Hopf bifurcation the small vortices play an important role and they can only be reproduced using meshes concentrated on the borders.

The influence of the power-law index is strong in both the first and second Hopf bifurcation. In both cases the pseudoplastic fluid reaches bifurcations first, while the dilatant reaches them later. The Re values

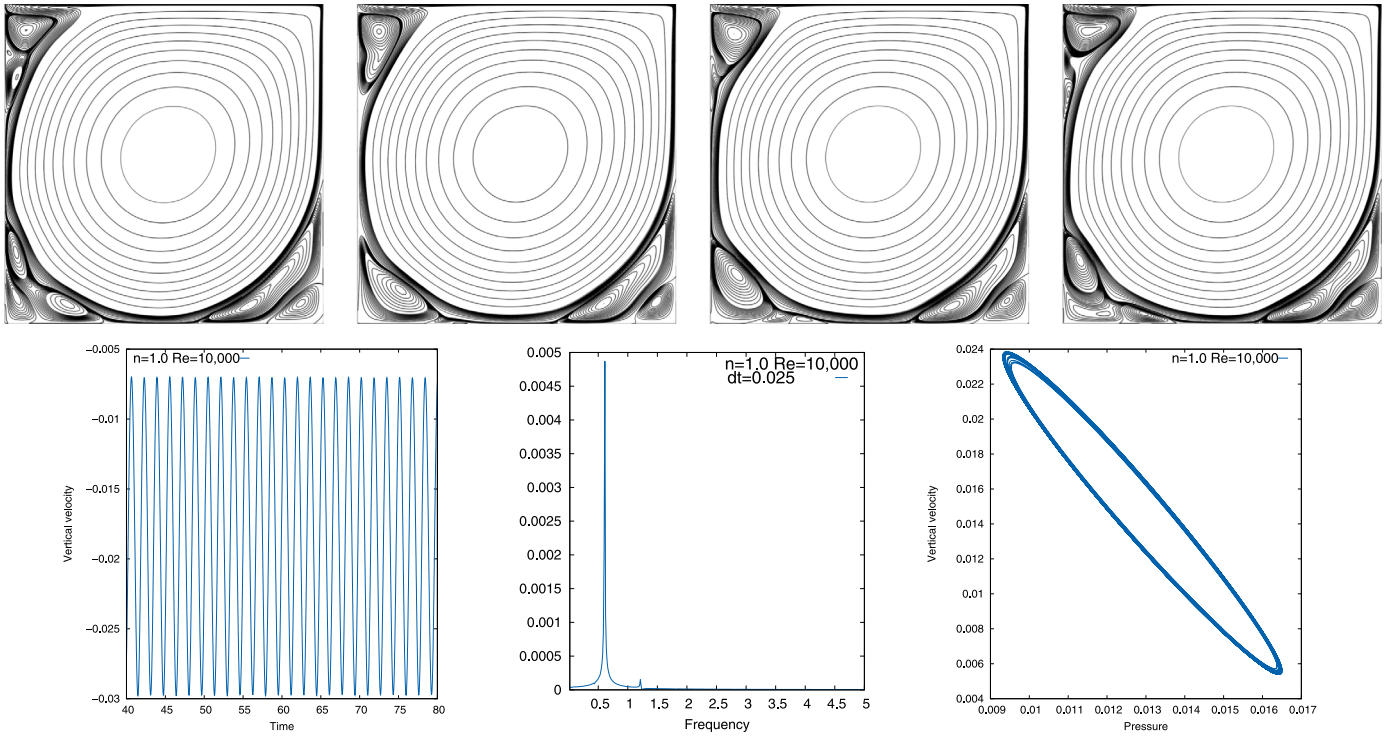

Fig. 19. Top: streamlines at four different times (t = 51.7, t = 52.1, t = 52.5 and t = 52.9), vertical velocity history (bottom left), Fourier frequency spectrum (bottom middle) and phase diagram (bottom right), at Re = 10, 000 for n = 1.

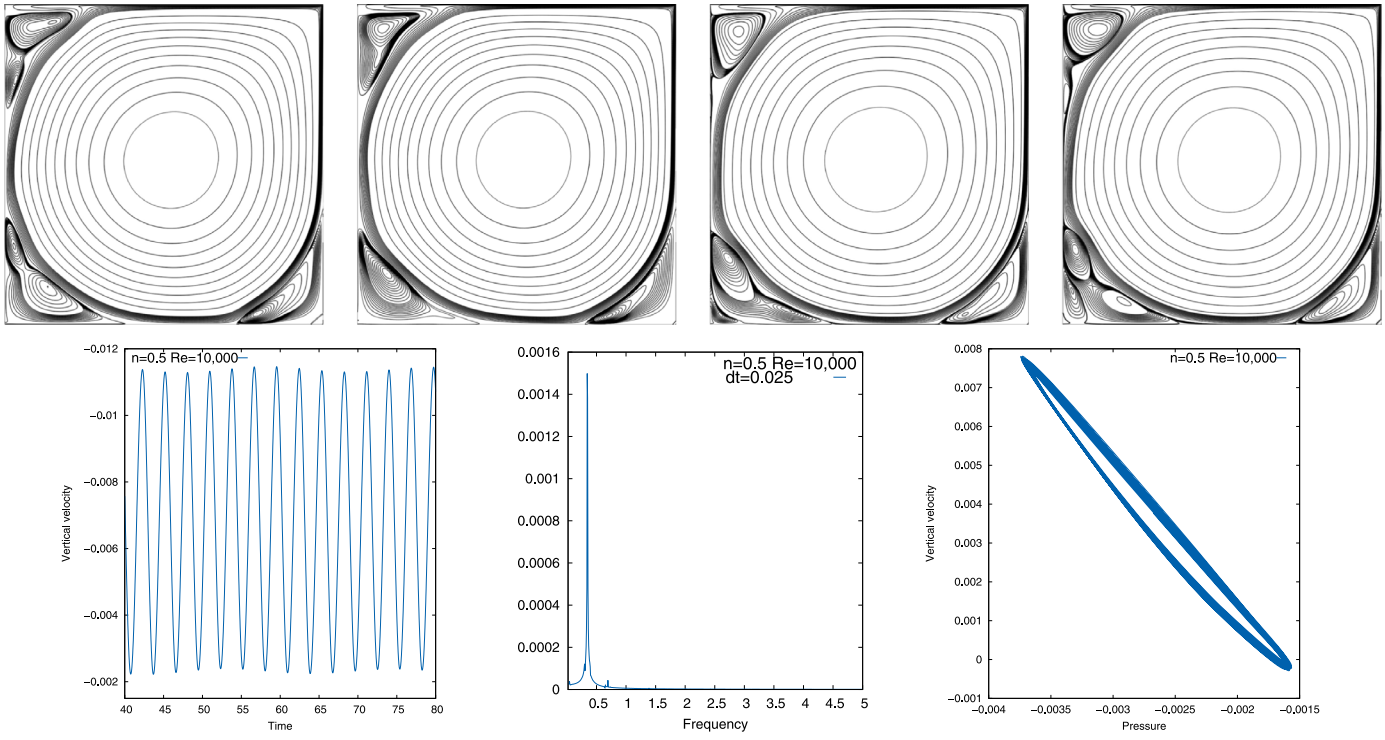

Fig. 20. Top: streamlines at four different times (t = 67.4, t = 68.2, t = 68.9 and t = 69.6), vertical velocity history (bottom left), Fourier frequency spectrum (bottom middle) and phase diagram (bottom right), at Re = 10, 000 for n = 0.5.

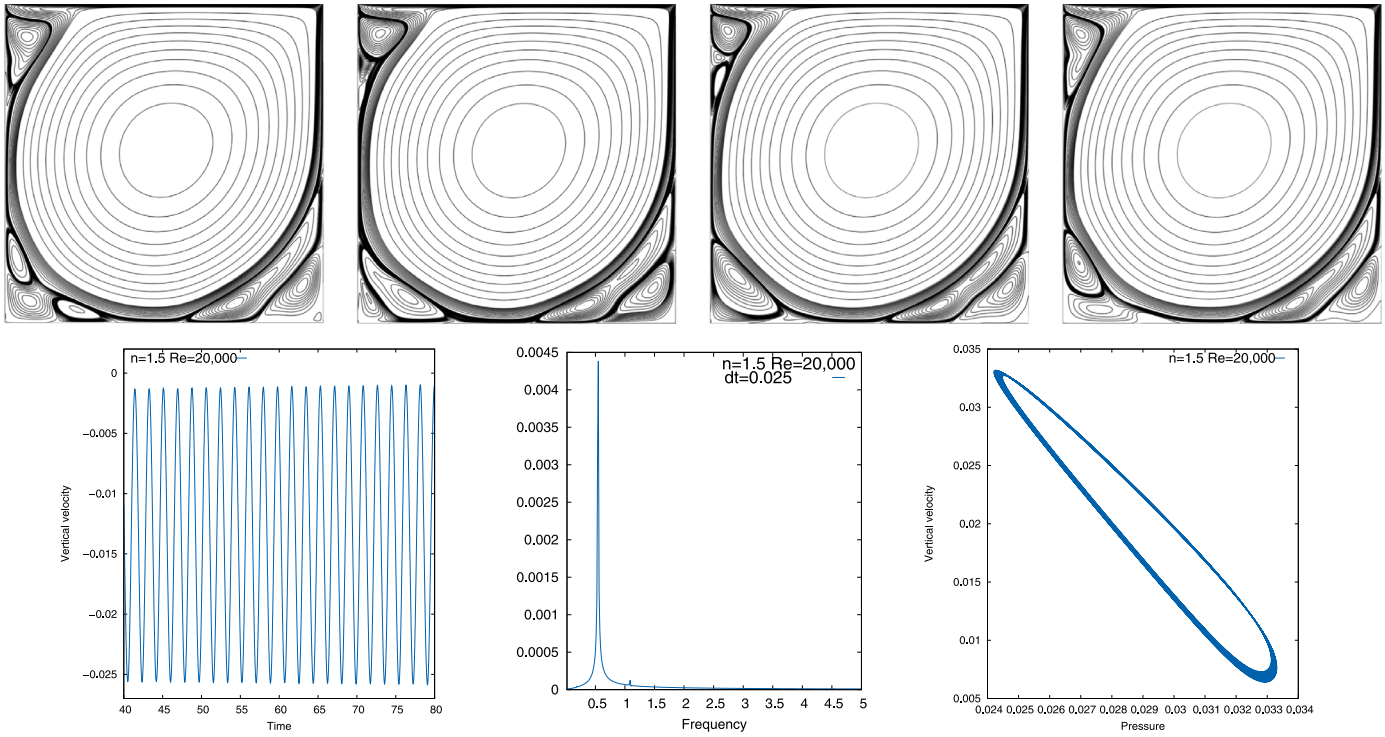

Fig. 21. Top: streamlines at four different times (t = 43.7, t = 44.2, t = 44.7 and t = 45.1), vertical velocity history (bottom left), Fourier frequency spectrum (bottom middle) and phase diagram (bottom right), at Re = 20, 000 for n = 1.5.

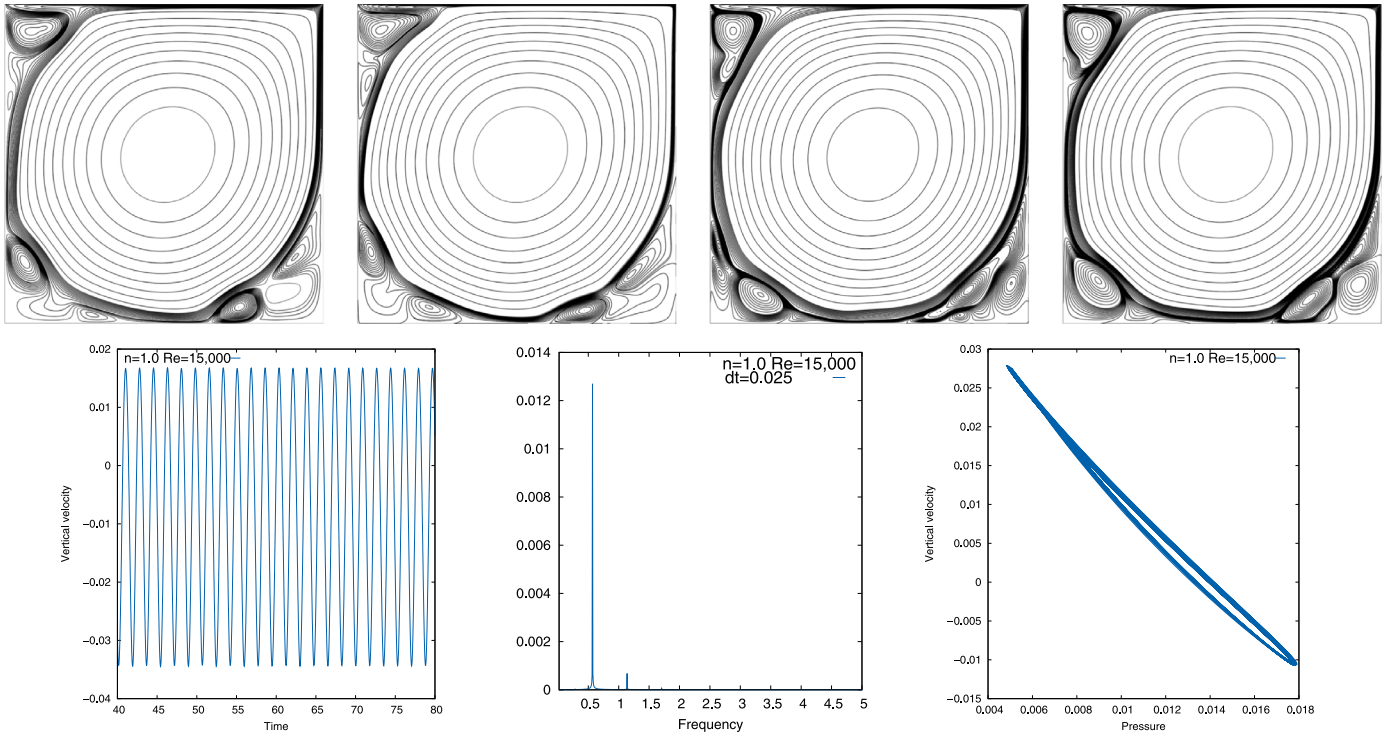

Fig. 22. Top: streamlines at four different times (t = 76.6, t = 77, t = 77.4 and t = 77.9), vertical velocity history (bottom left), Fourier frequency spectrum (bottom middle) and phase diagram (bottom right), at Re = 15, 000 for n = 1.

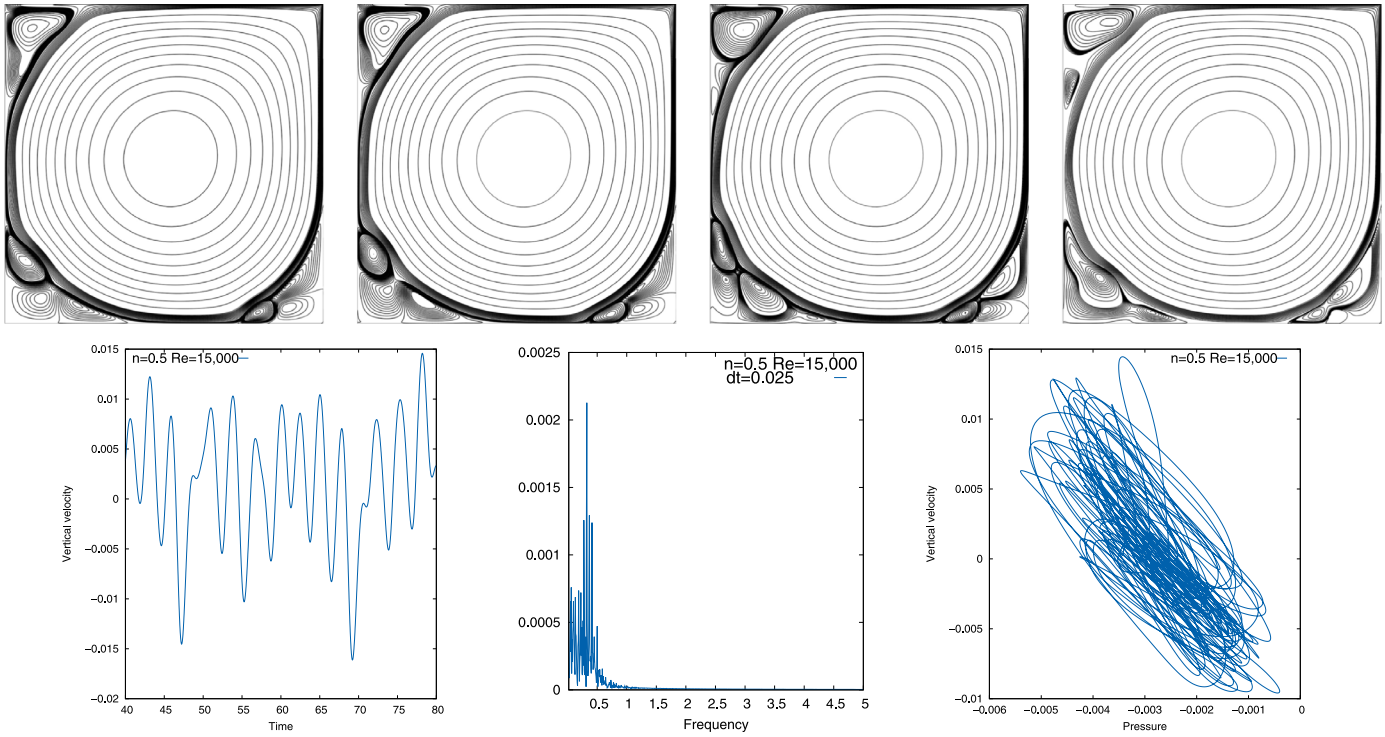

Fig. 23. Top: streamlines at four different times ($t = 53$, $t = 53.8$, $t = 55.2$ and $t = 55.9$), vertical velocity history (bottom left), Fourier frequency spectrum (bottom middle) and phase diagram (bottom right), at Re = 15, 000 for $n = 0.5$.

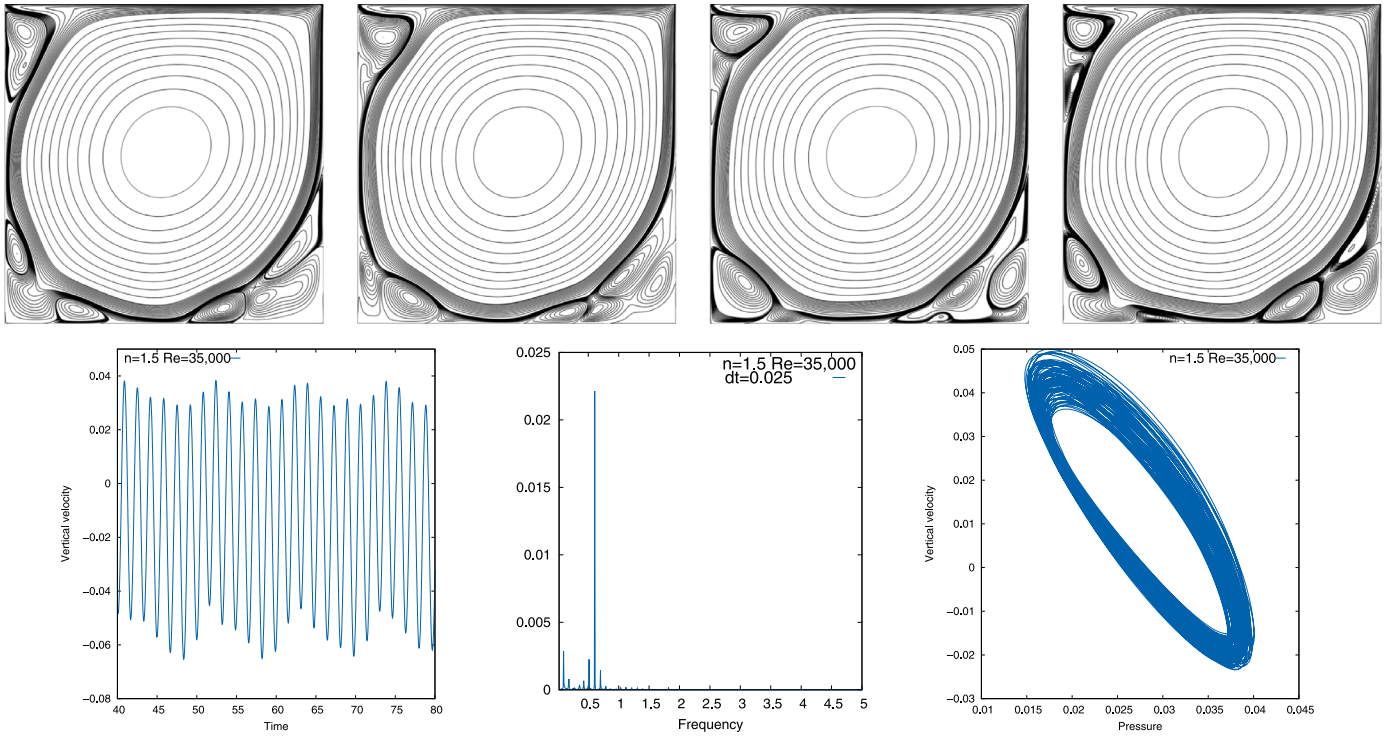

Fig. 24. Top: streamlines at four different times ($t = 71.1$, $t = 73.7$, $t = 75.9$ and $t = 76.3$), vertical velocity history (bottom left), Fourier frequency spectrum (bottom middle) and phase diagram (bottom right), at Re = 35, 000 for $n = 1.5$.

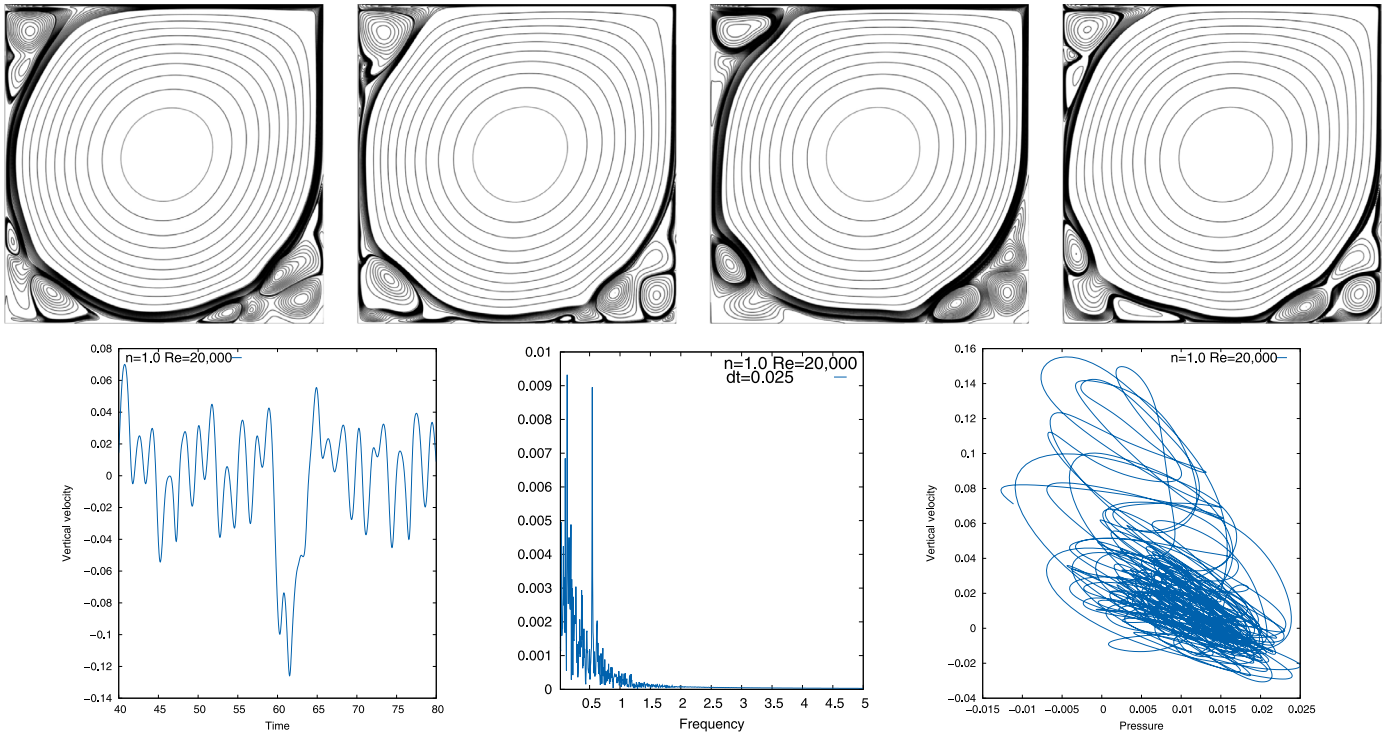

Fig. 25. Top: streamlines at four different times ($t = 74$, $t = 74.4$, $t = 74.8$ and $t = 75.4$), vertical velocity history (bottom left), Fourier frequency spectrum (bottom middle) and phase diagram (bottom right), at Re = 20, 000 for $n = 1$.

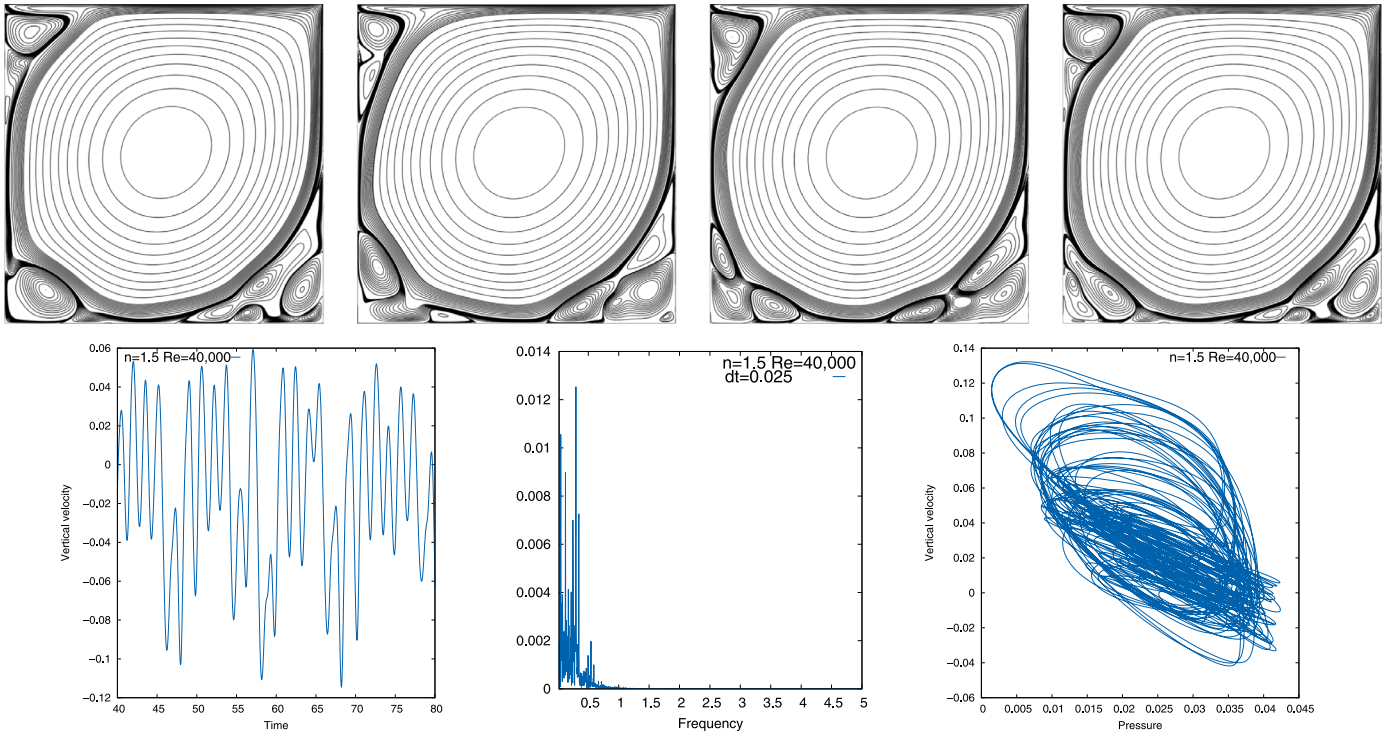

Fig. 26. Top: streamlines at four different times ($t = 73$, $t = 73.4$, $t = 73.8$ and $t = 74.1$), vertical velocity history (bottom left), Fourier frequency spectrum (bottom middle) and phase diagram (bottom right), at Re = 40, 000 for $n = 1.5$.

for which the bifurcations occur are extremely different, making this work a contribution to the study of non-Newtonian fluids.

Acknowledgments

This work has been partially funded by the Chilean Council for Scientific and Technological Research (CONICYT-FONDECYT 11160160). We also acknowledge the support received by the Scientific Research Projects Management Department of the Vice Presidency Research, Development and Innovation (DICYT-VRIDEI) at Universidad de Santiago de Chile in Proyecto Basal USA 1555 - Vridei 051716CSSSA_PUBLIC. Joan Baiges acknowledges the support of the Spanish Government through Ramón y Cajal grant RYC-2015-17367. R. Codina acknowledges the support received through the ICREA Academic Research Program.

Appendix A. Algorithm of the fully discrete and linearized problem

READ $\boldsymbol{u}_h^0$ (initial condition)
SET $p_h^0 = 0$
FOR, $j = 0, \ldots, N-1$ DO (temporal loop, N number of time steps)
  SET $i = 0$
  SET $\boldsymbol{u}_h^{j+1,0} = \boldsymbol{u}_h^j$ and $p_h^{j+1,0} = p_h^j$
  WHILE not converged DO:
    $i \leftarrow i + 1$
    SET advection velocity $\boldsymbol{a}_h^{j+1,i} = \boldsymbol{u}_h^{j+1,i-1}$
    COMPUTE $\eta^{j+1,i}$ (from 2.2)
    IF (OSS case)
      COMPUTE $P_h(\boldsymbol{R}_u^{j+1,i})$
    END IF
    COMPUTE α_1 and α_2 from Eq. (16) and (17)
    SOLVE FOR $\boldsymbol{u}_h^{j+1,i}$ and $p_h^{j+1,i}$ from Eq. (19) and (20)
    $\boldsymbol{u}_h^{j+1,i} \leftarrow \beta \boldsymbol{u}_h^{j+1,i} + (1-\beta)\boldsymbol{u}_h^{j+1,i-1}$
    $p_h^{j+1,i} \leftarrow \beta p_h^{j+1,i} + (1-\beta)p_h^{j+1,i-1}$
    CHECK convergence $|\boldsymbol{u}_h^{j+1,i} - \boldsymbol{u}_h^{j+1,i-1}| \leq 10^{-6}|\boldsymbol{u}_h^{j+1,i}|$ and $|p_h^{j+1,i} - p_h^{j+1,i-1}| \leq 10^{-6}|\boldsymbol{p}_h^{j+1,i}|$
  END WHILE
  SET converged values
  $\boldsymbol{u}_h^{j+1} = \boldsymbol{u}_h^{j+1,i}$
  $p_h^{j+1} = p_h^{j+1,i}$
END DO (temporal loop)

Algorithm 1. Fully discrete and linearized problem.

References

[1] N.O. Moraga, G.P. Parada, D.A. Vasco, Power law non-newtonian fluid unsteady conjugate three-dimensional natural convection inside a vessel driven by surrounding air thermal convection in a cavity, Int. J. Therm. Sci. 107 (2016) 247–258, http://dx.doi.org/10.1016/j.ijthermalsci.2016.04.007.
[2] A.H. Kong, A. Vega-Gálvez, N.O. Moraga, R. Lemus-Mondaca, Modelling of rheological behaviour of Pulps and Purées from fresh and Frozen-Thawed Murta (Ugni molinae Turcz) berries, Int. J. Food Eng. 8 (3) (2012) 1–24.
[3] A. Varshney, S. Gohil, B. Chalke, R. Bapat, S. Mazumder, S. Bhattacharya, S. Ghosh, Rheology of hydrating cement paste: crossover between two aging processes, Cem. Concr. Res. 95 (2017) 226–231, http://dx.doi.org/10.1016/j.cemconres.2017.02.034.
[4] P. Coussot, S. Proust, C. Ancey, Rheological interpretation of deposits of yield stress fluids, J. Nonnewton Fluid Mech. 66 (1) (1996) 55–70, http://dx.doi.org/10.1016/0377-0257(96)01474-7.
[5] J. Chen, X.-Y. Lu, W. Wang, Non-newtonian effects of blood flow on hemodynamics in distal vascular graft anastomoses, J. Biomech. 39 (11) (2006) 1983–1995, http://dx.doi.org/10.1016/j.jbiomech.2005.06.012.
[6] A. García-Abuín, D. Gómez-Díaz, J. Navaza, L. Regueiro, I. Vidal-Tato, Viscosimetric behaviour of hyaluronic acid in different aqueous solutions, Carbohydr. Polym. 85 (3) (2011) 500–505, http://dx.doi.org/10.1016/j.carbpol.2011.02.028.
[7] R.B. Bird, W.E. Stewart, E.N. Lightfoot, Transport Phenomena, second ed., Wiley, New York, 2002.
[8] R.P. Chhabra, J.F. Richardson, Non-Newtonian Flow and Applied Rheology, second ed., Elsevier Butterworth-Heinemann, 2008.
[9] M.D. Graham, Drag reduction and the dynamics of turbulence in simple and complex fluids, Phys. Fluids 26 (10130) (2014), http://dx.doi.org/10.1063/1.4895780.
[10] C.M. White, M.G. Mungal, Mechanics and prediction of turbulent drag reduction with polymer additives, Annu. Rev. Fluid Mech. 40 (2008) 235–256, http://dx.doi.org/10.1016/j.jnnfm.2013.09.007.
[11] N.O. Moraga, E.F. Castillo, C.P. Garrido, Non newtonian annular alloy solidification in mould, Heat Mass Transf. 48 (8) (2012) 1415–1424, http://dx.doi.org/10.1007/s00231-012-0983-0.
[12] B. Traore, C. Castelain, T. Burghelea, Efficient heat transfer in a regime of elastic turbulence, J. Nonnewton Fluid Mech. 223 (2015) 62–76, http://dx.doi.org/10.1016/j.jnnfm.2015.05.005.
[13] R. Whalley, W. Abed, D. Dennis, R. Poole, Enhancing heat transfer at the microscale using elastic turbulence, Theor. Appl. Mech. Lett. 5 (3) (2015) 103–106, http://dx.doi.org/10.1016/j.taml.2015.03.006.
[14] M.F. Letelier, D.A. Siginer, A. González, Elasto-viscoplastic fluid flow in tubes of arbitrary cross-section, Appl. Math. Model. 46 (2017) 572–580, http://dx.doi.org/10.1016/j.apm.2017.01.058.
[15] A. Chatterjee, Heat transfer enhancement in laminar impinging flows with a non-newtonian inelastic fluid, J. Nonnewton Fluid Mech. 211 (2014) 50–61, http://dx.doi.org/10.1016/j.jnnfm.2014.06.009.
[16] Y. Wang, C. Shu, L. Yang, H. Yuan, A decoupling multiple-relaxation-time lattice Boltzmann flux solver for non-newtonian power-law fluid flows, J. Nonnewton Fluid Mech. 235 (2016) 20–28, http://dx.doi.org/10.1016/j.jnnfm.2016.03.010.
[17] Q. Li, N. Hong, B. Shi, Z. Chai, Simulation of power-law fluid flows in two-dimensional square cavity using multi-relaxation-time lattice Boltzmann method, Commun. Comput. Phys. 15 (1) (2014) 265–284.
[18] E. Castillo, R. Codina, Stabilized stress-velocity-pressure finite element formulations of the Navier–Stokes problem for fluids with non-linear viscosity, Comput. Methods

Appl. Mech. Eng. 279 (2014) 554–578, http://dx.doi.org/10.1016/j.cma.2014.07.003.
[19] U. Ghia, K.N. Ghia, C.T. Shin, High-Re solutions for incompressible flow using the Navier–Stokes equations and a multigrid method, J. Comput. Phys. 48 (1982) 387–411, http://dx.doi.org/10.1016/0021-9991(82)90058-4.
[20] E. Wahba, Steady flow simulations inside a driven cavity up to Reynolds number 35,000, Comput. Fluids 66 (2012) 85–97, http://dx.doi.org/10.1016/j.compfluid.2012.06.012.
[21] K. Yapici, Y. Uludag, Finite volume simulation of 2-D steady square lid driven cavity flow at high Reynolds numbers, Braz. J. Chem. Eng. 30 (2013) 923–937.
[22] E. Erturk, T.C. Corke, C. Gökçöl, Numerical solutions of 2-d steady incompressible driven cavity flow at high Reynolds numbers, Int. J. Numer. Methods Fluids 48 (7) (2005) 747–774, http://dx.doi.org/10.1002/fld.953.
[23] E. Hachem, B. Rivaux, T. Kloczko, H. Digonnet, T. Coupez, Stabilized finite element method for incompressible flows with high Reynolds number, J. Comput. Phys. 229 (23) (2010) 8643–8665, http://dx.doi.org/10.1016/j.jcp.2010.07.030.
[24] S. García, Hopf bifurcations, drops in the lid-driven square cavity flow, Adv. Appl. Math. Mech. 1 (2009) 546–572.
[25] M. Escudier, F. Presti, S. Smith, Drag reduction in the turbulent pipe flow of polymers, J. Nonnewton Fluid Mech. 81 (3) (1999) 197–213, http://dx.doi.org/10.1016/S0377-0257(98)00098-6.
[26] J. Peixinho, C. Nouar, C. Desaubry, B. Théron, Laminar transitional and turbulent flow of yield stress fluid in a pipe, J. Nonnewton Fluid Mech. 128 (2) (2005) 172–184, http://dx.doi.org/10.1016/j.jnnfm.2005.03.008.
[27] M. Rudman, H. Blackburn, Direct numerical simulation of turbulent non-newtonian flow using a spectral element method, Appl. Math. Model. 30 (11) (2006) 1229–1248, http://dx.doi.org/10.1016/j.apm.2006.03.005. Selected papers from the Third International Conference on CFD in the Minerals and Process Industries
[28] A.A. Gavrilov, V.Y. Rudyak, Reynolds-averaged modeling of turbulent flows of power-law fluids, J. Nonnewton Fluid Mech. 227 (2016) 45–55, http://dx.doi.org/10.1016/j.jnnfm.2015.11.006.
[29] J. Singh, M. Rudman, H. Blackburn, A. Chryss, L. Pullum, L. Graham, The importance of rheology characterization in predicting turbulent pipe flow of generalized newtonian fluids, J. Nonnewton Fluid Mech. 232 (2016) 11–21, http://dx.doi.org/10.1016/j.jnnfm.2016.03.013.
[30] C.-H. Bruneau, M. Saad, The 2d lid-driven cavity problem revisited, Comput. Fluids 35 (3) (2006) 326–348, http://dx.doi.org/10.1016/j.compfluid.2004.12.004.
[31] A. Fortin, M. Jardak, R. Pierre, Localization of Hopf bifurcations in fluid flow problems, Int. J. Numer. Methods Fluids 24 (3) (1997) 1185–1210.
[32] A. Hajesfandiari, G.F. Dargush, A.R. Hadjesfandiari, Size-dependent fluid dynamics with application to lid-driven cavity flow, J. Nonnewton Fluid Mech. 223 (2015) 98–115, http://dx.doi.org/10.1016/j.jnnfm.2015.05.008.
[33] V. Girault, P. Raviart, Finite Element Methods for Navier–Stokes Equations: Theory and Algorithms, first ed., Springer-Verlag, Berlin Heideberg New York Tokio, 1986.
[34] R. Codina, A stabilized finite element method for generalized stationary incompressible flows, Comput. Methods Appl. Mech. Eng. 190 (20–21) (2001) 2681–2706, http://dx.doi.org/10.1016/S0045-7825(00)00260-7.
[35] O. Colomés, S. Badia, R. Codina, J. Principe, Assessment of variational multiscale models for the large eddy simulation of turbulent incompressible flows, Comput. Methods Appl. Mech. Eng. 285 (2015) 32–63.
[36] R.B. Bird, R.C. Amstrong, O. Hassager, Dynamics of Polymeric Liquids, vol.1: Fluid Mechanics, second ed., Wiley, New York, 1987.
[37] R. Owens, T. Phillips, Computational Rheology, Imperial College Press, London, 2002.
[38] R. Codina, S. Badia, J. Baiges, J. Principe, Variational multiscale methods in computational fluid dynamics, Encyclopedia of Computational Mechanics, (2017).
[39] T.J. Hughes, G.R. Feijóo, L. Mazzei, J.-B. Quincy, The variational multiscale method-a paradigm for computational mechanics, Comput. Methods Appl. Mech. Eng. 166 (1–2) (1998) 3–24.
[40] R. Codina, Analysis of a stabilized finite element approximation of the Oseen equations using orthogonal subscales, Appl. Numer. Math. 58 (3) (2008) 264–283, http://dx.doi.org/10.1016/j.apnum.2006.11.011.
[41] E. Castillo, R. Codina, Variational multi-scale stabilized formulations for the stationary three-field incompressible viscoelastic flow problem, Comput. Methods Appl. Mech. Eng. 279 (2014) 579–605.
[42] R. Codina, J. Principe, O. Guasch, S. Badia, Time dependent subscales in the stabilized finite element approximation of incompressible flow problems, Comput. Methods Appl. Mech. Eng. 196 (21–24) (2007) 2413–2430.
[43] R. Codina, Stabilized finite element approximation of transient incompressible flows using orthogonal subscales, Comput. Methods Appl. Mech. Eng. 191 (39) (2002) 4295–4321.
[44] C. Zhuo, C. Zhong, J. Cao, Filter-matrix lattice Boltzmann simulation of lid-driven deep-cavity flows, part ii-flow bifurcation, Comput. Math. Appl. 65 (12) (2013) 1883–1893.
[45] A. Brezillon, G. Girault, J. Cadou, A numerical algorithm coupling a bifurcating indicator and a direct method for the computation of hopf bifurcation points in fluid mechanics, Comput. Fluids 39 (7) (2010) 1226–1240.
[46] S. García, The lid-driven square cavity flow: from stationary to time periodic and chaotic, Commun. Comput. Phys. 2 (2007) 900–932.